Graphical Abstract

Accelerated Diffusion Weighted Magnetic Resonance Imaging at 7 T: Joint Reconstruction for Shift-Encoded Navigator-based Interleaved Echo Planar Imaging (JETS-NAViEPI)

Zhengguo Tan, Patrick Alexander Liebig, Robin Martin Heidemann, Frederik Bernd Laun, Florian Knoll

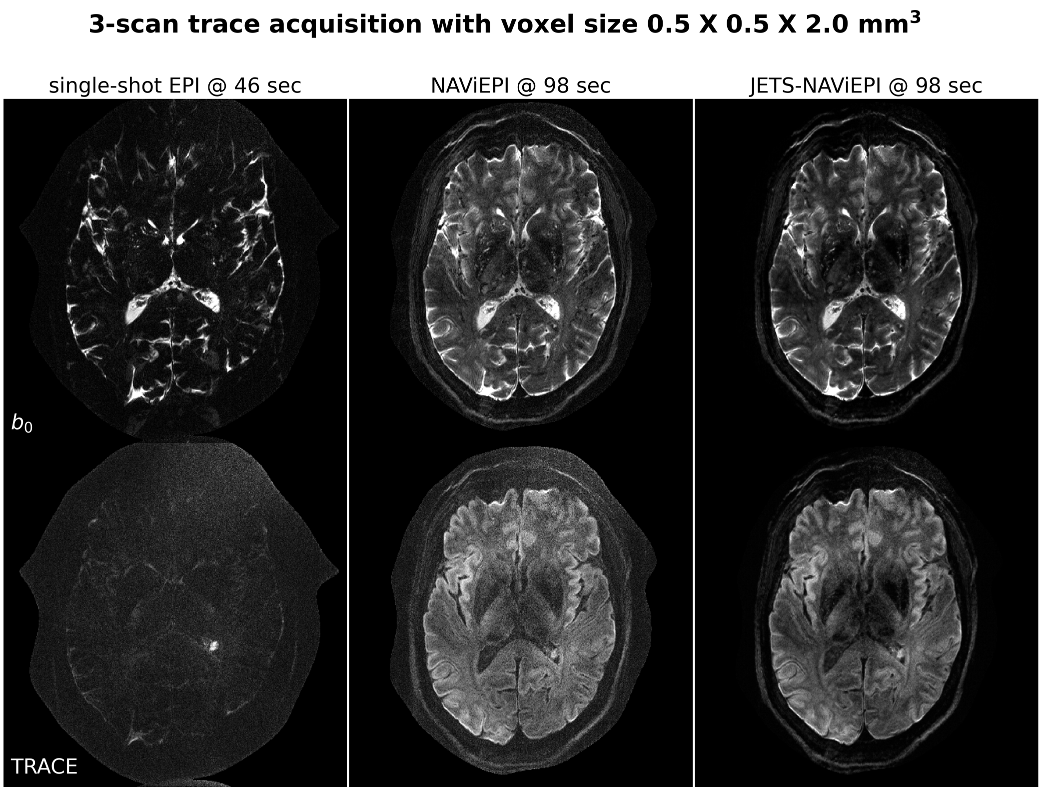

Highlights

Accelerated Diffusion Weighted Magnetic Resonance Imaging at 7 T: Joint Reconstruction for Shift-Encoded Navigator-based Interleaved Echo Planar Imaging (JETS-NAViEPI)

Zhengguo Tan, Patrick Alexander Liebig, Robin Martin Heidemann, Frederik Bernd Laun, Florian Knoll

- Navigator-based interleaved EPI acquisition with minimal distortion mismatch between echoes
- Novel accelerated diffusion acquisition with shifted phase encoding among diffusion directions for complementary k-q-space sampling at 7 T
- Generalized joint k-q-slice diffusion-weighted image reconstruction with overlapping locally low-rank regularization
- Efficient simultaneous multi-slice (SMS) image reconstruction
- 3-scan trace acquisition with the voxel size $0.5 \times 0.5 \times 2.0$ mm^3 and 60 slices at 1.5 min

Accelerated Diffusion Weighted Magnetic Resonance Imaging at 7 T: Joint Reconstruction for Shift-Encoded Navigator-based Interleaved Echo Planar Imaging (JETS-NAViEPI)

Zhengguo Tan[a], Patrick Alexander Liebig[b], Robin Martin Heidemann[b], Frederik Bernd Laun[c], Florian Knoll[a]

[a] *Department Artificial Intelligence in Biomedical Engineering (AIBE), Friedrich-Alexander University of Erlangen-Nuremberg, Erlangen, Germany*
[b] *Siemens Healthcare GmbH, Erlangen, Germany*
[c] *Institute of Radiology, University Hospital Erlangen, Friedrich-Alexander University of Erlangen-Nuremberg, Erlangen, Germany*

Abstract

The pursuit of high spatial-angular-temporal resolution for in vivo diffusion-weighted magnetic resonance imaging (DW-MRI) at ultra-high field strength (7 T and above) is important in understanding brain microstructure and function. Such pursuit, however, faces several technical challenges. First, increased off-resonance and shorter T_2 relaxation require faster echo train readouts. Second, existing high-resolution DW-MRI techniques usually employ in-plane fully-sampled multi-shot EPI, which not only prolongs the scan time but also induces a high specific absorption rate (SAR) at 7 T. To address these challenges, we develop in this work navigator-based interleaved EPI (NAViEPI) which enforces the same effective echo spacing (ESP) between the imaging and the navigator echo. First, NAViEPI renders no distortion mismatch between the two echoes, and thus simplifies shot-to-shot phase variation correction. Second, NAViEPI allows for a large number of shots (e.g. > 4) with undersampled iEPI acquisition, thereby rendering clinically-feasible high-resolution sub-milliemeter protocols. To retain signal-to-noise ratio (SNR) and to reduce undersampling artifacts, we developed a k_y-shift encoding among diffusion encodings to explore complementary k-q-space sampling. Moreover, we developed a novel joint reconstruction with overlapping locally low-rank regularization generalized to the multi-band multi-shot acquisition at 7 T (dubbed JETS-NAViEPI). Our method was demonstrated with experimental results covering 1 mm isotropic resolution multi b-value DWI and sub-millimeter in-plane resolution fast TRACE acquisition.

R248.Major.6

Keywords: Diffusion-weighted magnetic resonance imaging, Echo planar imaging, Navigator, Ultra-high field, Joint reconstruction, Low rank, Simultaneous multi slice

1. Introduction

Diffusion-weighted magnetic resonance imaging (DW-MRI) (Le Bihan et al., 1986; Merboldt et al., 1985) is a non-invasive modality that is sensitive to the intravoxel Brownian motion of water molecules. DW-MRI forms the basis for diffusion tensor imaging (DTI) (Basser et al., 1994; Mori et al., 1999) and high angular resolution diffusion imaging (HARDI) (Tuch et al., 2002), and has been widely used in acute brain ischemia diagnosis, in tumor detection and staging, and in neuroscience (Jones, 2010).

For DW-MRI acquisition, the commonly used pulse sequence is single-shot echo-planar imaging (SS-EPI) (Mansfield, 1977). SS-EPI is capable of rapidly acquiring one DW image per radio-frequency excitation at the order of 100 ms, and is thus motion robust. However, conventional SS-EPI, even with three-fold accelerated acquisition (Bammer et al., 2001) using parallel imaging (Roemer et al., 1990; Ra and Rim, 1993; Pruessmann et al., 1999; Griswold et al., 2002), still suffers from low spatial resolution and geometric distortions.

In the quest for high spatial-angular-temporal-resolution and minimal-geometry-distortion DW-MRI, tremendous efforts have been made. Techniques for the correction of image distortions induced by off-resonances and R249.Minor.5 eddy currents have been developed (Andersson et al., 2003). Furthermore, gSlider (Setsompop et al., 2018) with blipped-CAIPI (Setsompop et al., 2012) for simultaneous multi-slice (SMS) (Maudsley, 1980; Breuer et al., 2005) was proposed to achieve high-resolution DW-MRI. Advanced pulse sequences based on multi-shot EPI have also been developed, including but not limited to interleaved EPI (iEPI) (Butts et al., 1993), PROPELLER (Pipe et al., 2002), and readout-segmented EPI (rsEPI) (Porter and Heidemann, 2009; Heidemann et al., 2010).

Based on four-shot iEPI, multiplexed sensitivity encoding (MUSE) image reconstruction achieved DW-MRI with a sub-millimeter in-plane resolution and maximal b-value $800\,\mathrm{s/mm^2}$ at $3\,\mathrm{T}$ (Chen et al., 2013). The four-shot iEPI employed in MUSE acquired an in-plane fully-sampled k-space, except partial Fourier. Every shot (segment), corresponding to four-fold under-sampling, was then reconstructed via parallel imaging to obtain shot-to-shot phase variation. This indicates that increasing the number of shots in MUSE will result in higher undersampling per shot, and consequently, degrade shot phase estimation (Wu and Miller, 2017).

Alternatively, navigator-based iEPI acquisition has been proposed (Jeong et al., 2013; Dai et al., 2017, 2018). These proposals allow for a larger number of shots, and hence higher spatial resolution. However, due to the use of different ESP between the imaging echo and the navigator echo, these proposals suffered from geometric distortion mismatch between the two echoes and thus required specific compensation methods. In contrast, rsEPI (Porter and Heidemann, 2009; Heidemann et al., 2010) used the same readout segment for both echoes, and thus required no distortion correction of navigator echoes.

Beyond the MUSE-type parallel imaging reconstruction, compressed sensing (Lustig et al., 2007; Block et al., 2007) has been explored. For instance, multi-shot reconstruction techniques based on structured low-rank matrix completion (MUSSELS) (Mani et al., 2017; Bilgic et al., 2019) achieved 5-shot DW-MRI with 9-fold undersampling per shot. Recently, JULEP (Dai et al., 2023) incorporated explicit phase mapping into MUSSELS. These reconstruction techniques, i.e., MUSE, MUSSELS and JULEP, targeted the reconstruction of one DW image from interleaved EPI acquisition, and did not explore joint-k-q-space undersampling or reconstruction.

Joint-k-q-space undersampling can be achieved via proper regularization along the diffusion encoding direction. Relevant examples are diffusion undersampling with Gaussian process estimated reconstruction (DAGER) (Wu et al., 2019) and magnitude-based spatial-angular locally low-rank regularization (SPA-LLR) (Hu et al., 2020). However, DAGER addressed the reconstruction problem of single-shot EPI acquisition and SPA-LLR focused on the reconstruction of single-band and fully-sampled iEPI acquisition. R248.Major.2

In this work, we propose a Joint k-q-slice rEconsTruction framework for Shift-encoded NAVigator-based interleaved EPI at 7 T (dubbed JETS-NAViEPI). Our pulse sequence, NAViEPI, differs from most existing techniques. First, NAViEPI builds upon interleaved EPI, thereby allowing for fast and efficient k-space coverage. Second, inspired by rsEPI, NAViEPI ensures the same effective ESP between the imaging and the navigator echo, thereby minimizing geometric distortion and allowing for the use of a larger number of shots. NAViEPI essentially integrates the advantages of both iEPI and rsEPI. Third, NAViEPI utilizes undersampled multi-shot iEPI, thereby alleviating the SAR problem at 7 T. Fourth, NAViEPI shifts the k-space in-plane sampling pattern along the phase encoding (k_y) direction. This shifting creates complementary k-q-space sampling, which leads to the possibility of our joint k-q-slice reconstruction. Specifically, we employ spatial-diffusion overlapping LLR regularization to jointly reconstruct all diffusion encodings and multi-band slices. In vivo experiments at 7 T and comparisons with other techniques demonstrate the efficiency of our proposed method in achieving high spatial resolution DW-MRI at ultra-high field.

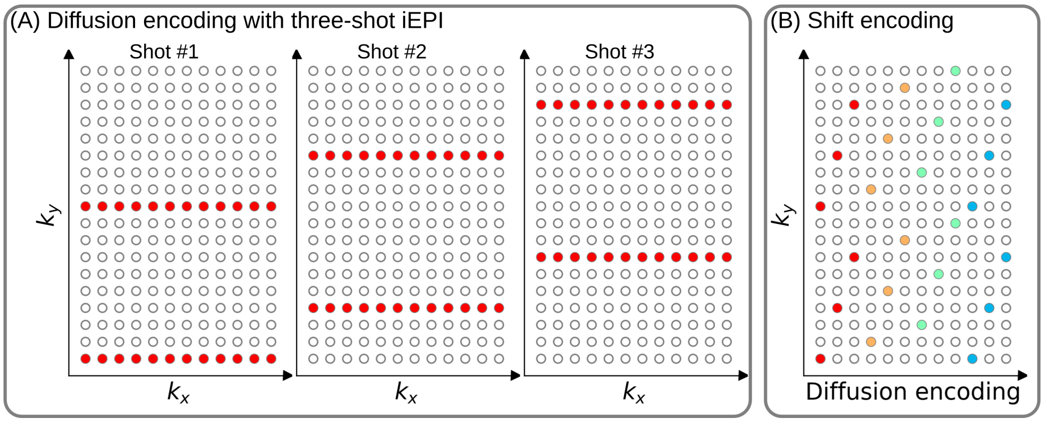

Figure 1: (A) An example DW-MRI acquisition with three-shot interleaved EPI acquisition. (B) The proposed k_y shifted diffusion encoding scheme. This example employs three shots per DW image. Therefore, every three columns have the same color.

2. Materials and methods

2.1. Multi-band shift-encoded iEPI acquisition

Fig. 1 (A) displays the diffusion-weighted image acquisition based on three-shot interleaved EPI with three-fold in-plane undersampling. Conventionally, such a sampling pattern is repeated for all diffusion directions. In contrast, we propose the k_y-shifted diffusion encoding, as shown in Fig. 1 (B). The interleaved EPI sampling pattern is shifted by one k_y line per diffusion direction, with the cycling period being the in-plane undersampling factor.

It is worth noting that, as shown in Fig. 1 (A), the undersampling factor of one segment is $R_{\text{in-plane}} \times N_{\text{shot}}$ (ignore multi-band undersampling here), yielding nine-fold in-plane undersampling in this example. In other words, the undersampling factor per segment linearly scales up with the number of shots. Consequently, conventional self-gating reconstruction techniques, e.g. MUSE, suffer from degraded shot-to-shot phase estimation, which in

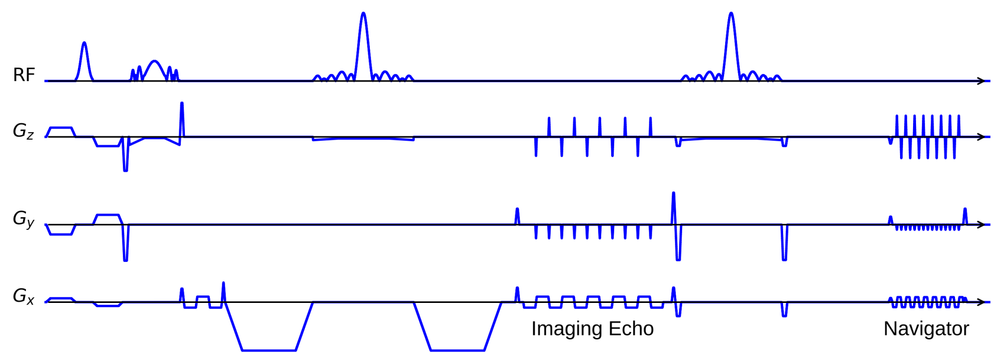

Figure 2: The NAViEPI sequence diagram. SMS is utilized for the acquisition of both imaging and navigator echoes. While the acceleration factor per navigator is the same as listed in Table 1, the acceleration factor per imaging echo is in addition linearly scaled by the number of shots.

turn limits the number of shots and spatial resolution.

2.2. NAViEPI: Navigator-based iEPI with consistent effective ESP between the imaging and the navigator echo - where iEPI meets rsEPI

Instead of the self-gated MUSE with in-plane fully-sampled iEPI and a limited number of shots, We propose NAVigator-based interleaved EPI (NAViEPI), as illustrated in Fig. 2. Inspired by rsEPI (Porter and Heidemann, 2009), NAViEPI enforces a consistent effective ESP between the imaging and the navigator echo, thereby minimizing distortion mismatch between the two echoes.

Since one imaging echo presents one segment in multi-shot EPI acquisition, its effective ESP is defined as

$$\mathrm{ESP}_{\mathrm{eff}} = \frac{\mathrm{ESP}}{R_{\text{in-plane}} \times N_{\text{shot}}} \tag{1}$$

Here, a larger number of shots (segments) increases the undersampling factor per segment (see Fig. 1), but decreases the effective ESP. Since the navigator echo is acquired for each segment, its in-plane undersampling factor equals $R_{\text{in-plane}}$. Therefore, the effective ESP of the navigator echo must match that of the imaging echo, as given in Eq. (1). With a matching effective ESP, the base resolution of the navigator echo can then be determined.

2.3. In vivo acquisition protocols

We implemented multiple in-vivo acquisition protocols at a clinical 7 T MR system (MAGNETOM Terra, Siemens Healthineers, Erlangen, Germany) equipped with a 32-channel head coil (Nova Medical, Wilmington, MA, USA) and the XR-gradient system (maximum gradient strength 80 mT/m with a peak slew rate of 200 T/m/s). To calibrate coil sensitivity maps, reference scans employed a gradient-echo (GRE) sequence. Spectral fat saturation and mono-polar diffusion-encoding gradients were used. The phase-encoding direction was selected as anterior-to-posterior.

Table 1: NAViEPI acquisition protocols

Protocol	**1.0 mm isotropic**		**sub-millimeter**	
	#1	#2	#3	#4
Diffusion mode	MDDW [(1)]		3-scan trace	
Diffusion scheme	monopolar			
Diffusion direction	20	114	3	
b-value (s/mm^2)	1000	3-shell [(2)]	1000	
b_0	0	12	1	
FOV (mm^2)	200	214	220	
In-plane resolution (mm^2)	1.0		0.5	
Slice thickness (mm)	1.0		2.0	
Slices	141	114	60	
Navigator	No	No	Yes	No
Shots	4	2	5	1
TR (ms)	7700	5200	4400	8000
TEs (ms)	67	66	58/95.1	143
ESP (ms)	1.02	0.81	1.52	1.48
Bandwidth (Hz/Pixel)	1086	1460	758	
Partial Fourier	6/8			
Acceleration [(3)]	1×3	3×3	3×2	
TA (min) [(4)]	10 : 42	22 : 25	1 : 38	0 : 46

[(1)] MDDW: Multi-direction diffusion weighting;

[(2)] 3-shell: 20, 30, and 64 directions with b-values of 1000, 2000,and 3000 s/mm^2, respectively;

[(3)] Acceleration: Both in-plane and slice undersampling can be employed, denoted as ($R_{\text{in-plane}} \times R_{\text{slice}}$);

[(4)] TA: Total acquisition time.

This study was approved by the local ethics committee. Three volunteers with informed consent obtained before scanning participated in this study. Detailed acquisition protocols are listed in Table 1.

2.3.1. *20-diffusion-direction acquisition at* 1 mm *isotropic resolution*

As listed in Table 1, Protocol #1 with four-shot iEPI and without in-plane undersampling was implemented. This protocol represents the acquisi- R248.Major.1a tion scheme employed in many existing multi-shot reconstruction techniques, (e.g., MUSE, SPA-LLR, and JULEP). The acquired data from this protocol served as ground truth. Different reconstruction methods, specifically JETS, MUSE, and JULEP were compared. We compared with JULEP instead of R249.Minor.6 MUSSELS, because JULEP uses not only structured low-rank constraints R248.Major.3a but also explicit phase mapping.

We then retrospectively reduced the four-shot data to only one shot per diffusion encoding without and with the proposed k_y shifting to simulate four-fold in-plane undersampling. JETS reconstruction was performed on R248.Major.1b the fully-sampled data and the retrospectively undersampled data to validate the proposed k_y-shifted acquisition. R248.Major.1c

2.3.2. *Three-shell acquisition at* 1 mm *isotropic resolution*

Protocol #2 in Table 1 was implemented for multi-shell diffusion tensor imaging (DTI) (Basser et al., 1994). We acquired a total of 114 diffusion R248.Major.3c directions, whereas b_0 measurements were interspersed every ten diffusion directions. This protocol was used to demonstrate the capability of of JETS in achieving high spatial-angular-temporal resolution.

2.3.3. 3-scan trace acquisition at $0.5 \times 0.5 \times 2.0$ mm^3 voxel size

As listed in Table 1, Protocol #3 was implemented based on NAViEPI with five shots per diffusion encoding. This protocol was compared against single-shot EPI (Protocol #4) with the same spatial resolution and acceleration, such as to demonstrate the sampling efficiency of NAViEPI.

2.4. Forward modeling

Our proposed acquisition method yields multi-dimensional multi-band k-space data $\mathbf{y}_{c,q,s}$, where c, q, s denotes the index of the coil sensitivity map, the diffusion encoding, and the shot, respectively. Acquisition modeling needs to consider several aspects.

First, the acquired k-space data $\mathbf{y}$ is mapped from individual shot images $\mathbf{x}_{q,s,z}$ via the forward model,

$$\begin{aligned} \mathbf{y}_{c,q,s} &= \mathbf{P}_{q,s}\mathbf{\Sigma}\mathbf{\Theta}_z\mathbf{F}\mathbf{S}_c\mathbf{x}_{q,s,z} \\ \mathbf{y} &\coloneqq \mathbf{E}_1\mathbf{x} \end{aligned} \tag{2}$$

Here, the encoding matrix $\mathbf{E}_1$ comprises a chain of linear operators. Every shot image $\mathbf{x}$ is point-wise multiplied by a set of coil sensitivity maps ($\mathbf{S}$) and Fourier transformed ($\mathbf{F}$). The output is then point-wise multiplied by the multi-slice phase map ($\mathbf{\Theta}$) with z the slice index in simultaneously excited slices. This operator shifts individual slice along the phase-encoding direction via varying phase modulation (Breuer et al., 2005). The SMS k-space data is then summed (collapsed, $\mathbf{\Sigma}$) along the slice dimension and masked (point-wise multiplied, $\mathbf{P}$) by the sampling pattern of each diffusion encoding and shot.

Second, for diffusion MRI based on multi-shot EPI, multiple shots acquired for a given diffusion encoding need to be combined as one DW image ($\tilde{\mathbf{x}}$). One possibility is to perform magnitude average (Chen et al., 2013) or root-sum-squares (RSS) (Mani et al., 2017) of shot images. This method R249.Minor.7 is robust to in-plane motion, but sub-optimal concerning SNR (Guhaniyogi et al., 2016). Alternatively, shot combination can be done via shot-to-shot phase variation correction (Liu et al., 2005; Chen et al., 2013). This can be incorporated into our formulation as point-wise multiplication between the R249.Minor.8 shot-to-shot phase variation ($\mathbf{\Phi}$) and the DW image ($\tilde{\mathbf{x}}$),

$$\mathbf{x}_{q,s,z} = \mathbf{\Phi}_{q,s,z} \tilde{\mathbf{x}}_{q,z} \tag{3}$$

Note that $\tilde{\mathbf{x}}$ can be obtained by applying the adjoint of $\mathbf{\Phi}$ to $\mathbf{x}$. In MUSE, $\mathbf{\Phi}$ is obtained by parallel imaging reconstruction of all shots with subsequent phase smoothing of every shot image. Based on this phase correction, the complete forward model follows

$$\mathbf{y} \coloneqq \mathbf{E}_2 \tilde{\mathbf{x}} = \mathbf{E}_1 \mathbf{\Phi} \tilde{\mathbf{x}} \tag{4}$$

where the encoding matrix $\mathbf{E}_2$ comprises the chain of the shot-to-shot phase variation $\mathbf{\Phi}$ and the encoding matrix $\mathbf{E}_1$. We implemented these two encoding operators in SigPy (Ong and Lustig, 2019).

2.5. Joint k-q-slice reconstruction

Based on the generalized forward models in Eqs. (2) and (4), our proposed joint k-q-slice reconstruction can be formulated as a three-step approach.

I. **Navigator echo reconstruction**. The acquisition of navigator echoes follows the forward model in Eq. (2), so the reconstruction of navigator echoes can be formulated as:

$$\text{argmin}_{\mathbf{x}} \|\mathbf{y} - \mathbf{E}_1\mathbf{x}\|_2^2 + \lambda\mathbf{R}(\mathbf{x}) \tag{5}$$

where $\mathbf{R}(\mathbf{x})$ denotes the regularization functional with the regularization strength λ. In this work, ℓ^2 regularization was used, i.e., $\mathbf{R}(\mathbf{x}) = \|\mathbf{x}\|_2^2$. In the case of self-navigating (i.e., no navigator acquired) as Protocol #2, the central k-space region (i.e., 1/4 of the full image matrix) of each segment is used as $\mathbf{y}$ in Eq. (5).

II. **Iterative phase smoothing**. Shot-to-shot phase variation was extracted from the reconstructed navigator echo phases. Assuming that phase images are spatially smooth (Chen et al., 2013; Dai et al., 2023), we employed the iterative approach to smooth phase,

$$\mathbf{x}^{(k+1)} = \mathbf{F}^{-1}\mathcal{H}\mathbf{F}\mathbf{x}^{(k)} \tag{6}$$

where the index k denotes the phase smoothing iteration step, and $x^{(0)}$ is then the reconstructed navigator image from Step I. $\mathcal{H}$ is the Hanning window. R248.Minor.12

III. **Shot-combined reconstruction**. Joint reconstruction of all DW images using the shot-combined forward model $\mathbf{E}_2$ with shot-to-shot phase variation from Step II reads:

$$\text{argmin}_{\tilde{\mathbf{x}}} \|\mathbf{y} - \mathbf{E}_2\tilde{\mathbf{x}}\|_2^2 + \lambda \|\mathbf{T}(\tilde{\mathbf{x}})\|_* \tag{7}$$

Here, LLR regularization was employed in the local spatial-diffusion matrices, based on the theory of partially separable functions (Liang, 2007; Trzasko and Manduca, 2011; Zhang et al., 2015). $\mathbf{T}$ represents a linear

operator that firstly slides a local patch window through all DW images and then flattens every set of local patches to construct two-dimensional (2D) spatial-diffusion matrices. The spatial dimension equals the block R248.Minor.6
size, and the diffusion dimension is the number of diffusion encodings. $\|\mathbf{T}(\tilde{\mathbf{x}})\|_*$ is the nuclear norm, i.e. the sum of singular values of a spatial-diffusion matrix. This nuclear norm regularization was accomplished via singular value thresholding (SVT) of each spatial-diffusion matrix R249.Minor.9
(Cai et al., 2010). After SVT, the adjoint of $\mathbf{T}$, $\mathbf{T}^H$, was needed to reorder pixel values from the spatial-diffusion matrices back to DW images. To alleviate checkerboard artifacts induced by LLR regularization with non-overlapping blocks (Hu et al., 2020), we employed overlapping blocks. In this case, values from overlapping positions are summed up to the output of $\mathbf{T}^H$. To enable the correct use of $\mathbf{T}^H$, we element-wise divided the output of $\mathbf{T}^H$ by a scaling matrix. This matrix was obtained via $\mathbf{T}^H(\mathbf{T}(\mathbf{1}))$, where $\mathbf{1}$ denotes the matrix of all ones with the same shape as the input $\mathbf{x}$.

2.6. Reconstruction

The acquired raw data was read in by twixtools (`https://github.com/pehses/twixtools`). Ramp-sampling regridding and FOV/2-ghost correction were also performed in twixtools. Subsequently, coil sensitivity maps were computed from reference scans using ESPIRiT (Uecker et al., 2014) in SigPy (Ong and Lustig, 2019).

With this pre-processing as well as the implemented forward models and proximal operator, the inverse problem in Eq. (7) was solved by the alternating direction method of multipliers (ADMM) (Boyd et al., 2010).

ADMM solves the minimization problems in an alternating update scheme,

$$\begin{cases} \mathbf{x}^{(k+1)} := \underset{\mathbf{x}}{\operatorname{argmin}} \left\| \mathbf{y} - \mathbf{E}(\mathbf{x}) \right\|^2 + \rho/2 \left\| \mathbf{T}\mathbf{x} - \mathbf{z}^{(k)} + \mathbf{u}^{(k)} \right\|_2^2 \\ \mathbf{z}^{(k+1)} := \mathcal{T}_{\lambda/\rho}(\mathbf{T}\mathbf{x}^{(k+1)} + \mathbf{u}^{(k)}) \\ \mathbf{u}^{(k+1)} := \mathbf{u}^{(k)} + \mathbf{T}\mathbf{x}^{(k+1)} - \mathbf{z}^{(k+1)} \end{cases} \tag{8}$$

where k denotes the ADMM iteration. $\mathbf{z}$ is the auxiliary variable ($\mathbf{z} = \mathbf{T}\mathbf{x}$), and $\mathbf{u}$ is the Lagrangian multipliers. Importantly, when solving Eq. (2), $\mathbf{x}$ denotes shot images and $\mathbf{E}$ denotes $\mathbf{E}_1$ in Eq. (8). In contrast, $\mathbf{x}$ denotes shot-combined images and $\mathbf{E}$ denotes $\mathbf{E}_2$ when solving Eq. (4). $\mathbf{x}$ can be solved using linear least square algorithms, e.g. conjugate gradients (Hestenes and Stiefel, 1952), while $\mathbf{z}$ is updated via singular value thresholding ($\mathcal{T}$) with the thresholding parameter λ/ρ. The coupling parameter ρ is effective in both the update of $\mathbf{x}$ and $\mathbf{z}$. It acts as Tikhonov regularization strength when updating $\mathbf{x}$, but also inversely scales the thresholding strength when updating $\mathbf{z}$.

In this work, 15 ADMM iterations with $\rho = 0.05$ and $\lambda = 0.08$ were used. All reconstructions were done on a single A100 SXM4/NVLink GPU with 40 GB memory (NVIDIA, Santa Clara, CA, USA).

We compared our proposed joint reconstruction with established multi-shot reconstruction techniques, specifically, MUSE (Chen et al., 2013) and JULEP (Dai et al., 2023), hosted on GitHub by Dr. Dai (Dai et al., 2023). Further, we performed the local-PCA denoising (Cordero-Grande et al., 2019) as implemented in MRtrix (Tournier et al., 2019) on the MUSE reconstructed complex DW images.

The in vivo data acquired from Protocol #2 in Table 1 consisted of 126 diffusion directions, which exceeds the available GPU memory. Therefore, the 126 data volumes were uniformly split into three parts for our JETS reconstruction with a LLR block width of 6 and the LLR regularization in both Steps I and III in Section 2.5. In addition, MUSE reconstruction was also performed, followed by the local-PCA denoising. Reconstructed DWIs were then processed by DiPy (Garyfallidis et al., 2014) to obtain color-coded fractional anisotropy (cFA) maps.

3. Results

3.1. Iterative smoothing of shot-to-shot phase variation

Navigators were acquired with the acceleration rate as listed in Table 1. Besides, the base resolution of navigators (e.g. 32 in Protocol #3 in Table 1) was smaller than imaging echoes. As a result, reconstructed navigator phases (refer to the first column in Fig. 3) from Step I in Section 2.5 are not spatially smooth. Such phases, when used in the shot-combined reconstruction, result in signal void artifacts in DW images. To address this problem, we utilized the iterative smoothing procedure. As shown in Fig. 3, the ripple-like phase artifact disappears after five iterations. It can also be seen that such an iterative procedure retains the shot-to-shot phase variation. R249.Minor.11 – 12

3.2. Comparison to MUSE and JULEP with four-shot iEPI acquisition

The iterative phase smoothing was also applicable to MUSE-type self-navigating reconstruction, where shot phases were reconstructed from imaging echoes. Fig. 4 compares our proposed JETS with MUSE (Chen et al., 2013), MUSE with complex-valued local-PCA denoiser (Cordero-Grande et al., 2019), and JULEP (Dai et al., 2023). The residual noise from MUSE can be largely removed by the denoiser. However, when compared to JETS, the denoiser shows residual noise patterns within the globus pallidus (indicated by the red arrow). JETS also shows better denoising than JULEP. The reason is that JETS enforces spatial-diffusion regularization, whereas JULEP formulates structured low-rank regularization of the four shots for one diffusion encoding.

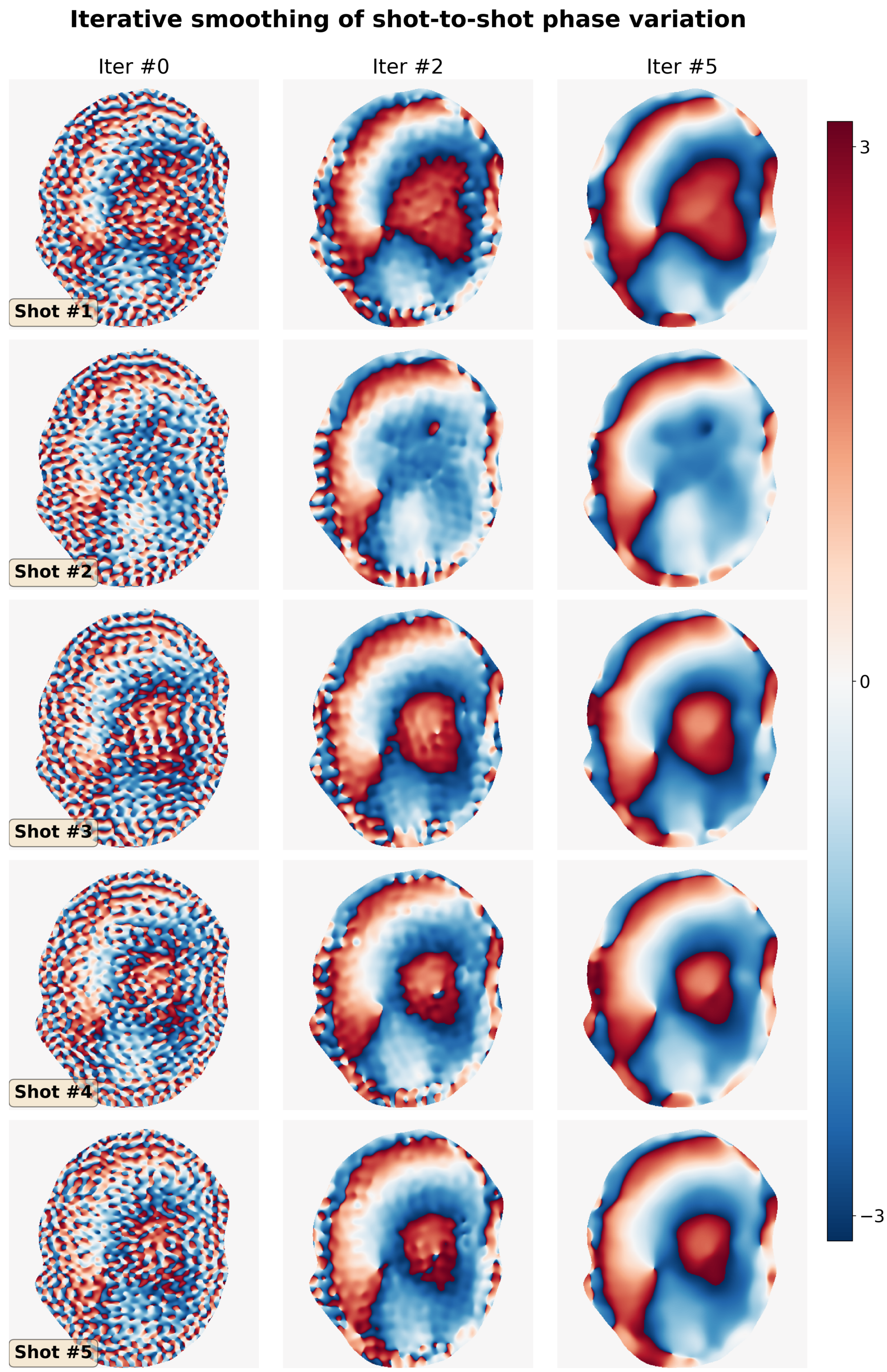

Figure 3: Iterative smoothing of shot-to-shot phase variation according to Eq. (6). Navigators from Protocol #3 were reconstructed based on Step I in Section 2.5 and then used as the input (iter #0, left column).

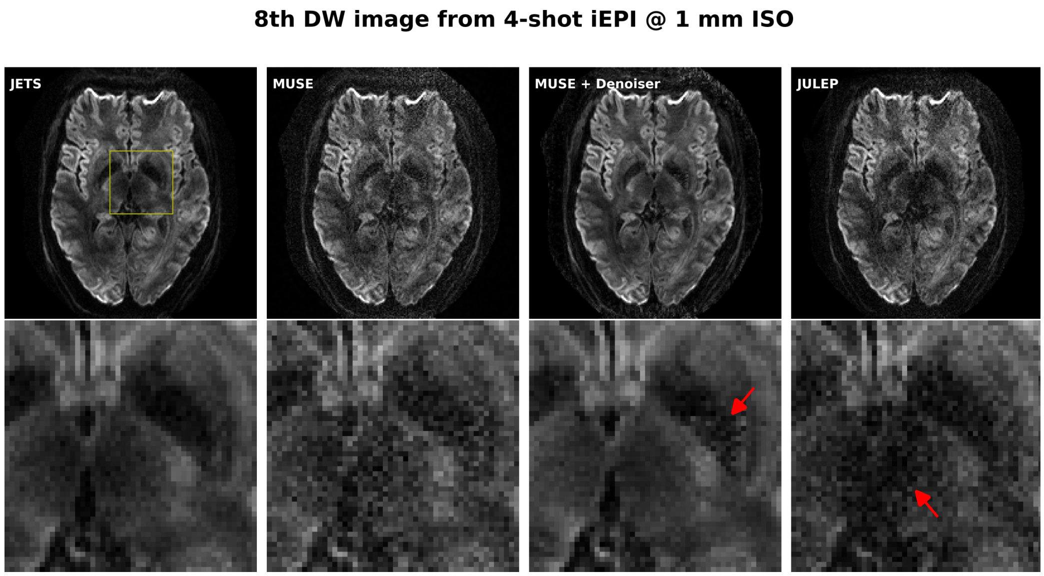

Figure 4: Reconstructed DW images (the 8th diffusion encoding) based on 4-shot iEPI acquisition with 1 mm isotropic resolution (Protocol #1 in Table 1). Four reconstruction methods are compared (from left to right): JETS, MUSE, MUSE with denoiser, and JULEP. The 2nd row displays the magnified views of the yellow square. The image from the denoiser (3rd column) shows residual noise patterns within the globus pallidus (indicated by the red arrow). The JULEP reconstruction (4th column) shows signal dropout in the central region (indicated by the red arrow).

R249.Minor.13

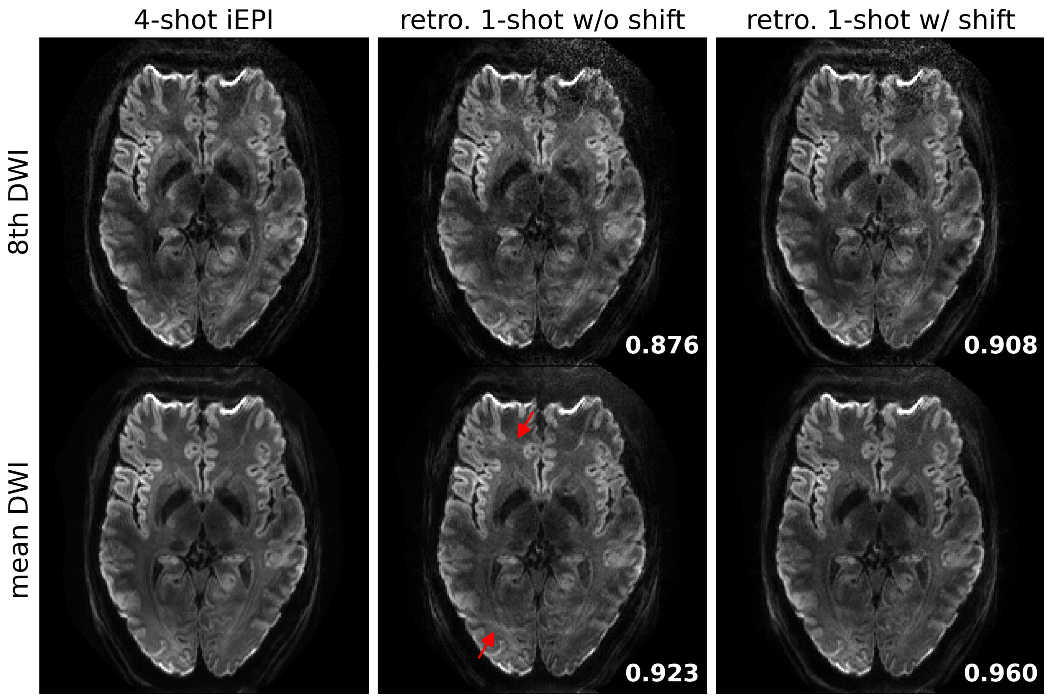

Figure 5: Quantitative validation of the proposed k_y-shift enoding sampling pattern based on 4-shot iEPI acquisition with 1 mm isotropic resolution (Protocol #1 in Table 1). (Top) the 8th diffusion encoding and (bottom) mean DWI over 20 diffusion encodings. (1st column) JETS reconstruction of 4-shot iEPI acquisition is used as the ground truth. The 2nd and the 3rd column displays JETS reconstruction of retrospectively undersampled 1-shot acquisition without and with k_y shifting, respectively. Residual aliasing artifacts are visible in the reconstruction without k_y shifting, as indicated by the red arrows. Structural similarity (SSIM) values are computed and displayed in the bottom right corners.

R249.Minor.14 – 16

3.3. Retrospectively undersampling from the four-shot iEPI acquisition

JETS reconstruction results on the four-shot prospectively fully-sampled data from Protocol #1 in Table 1, as well as on the retrospectively undersampled one-shot data without and with the proposed k_y shift are displayed in Fig. 5. Residual aliasing artifacts are visible in the reconstruction without k_y shifting, as indicated by the red arrows. In contrast, the k_y shifting scheme R249.Minor.17, supplies a complementary k-q-space sampling pattern, which is beneficial for 18, 20 joint reconstructions such as JETS. As shown in Fig. 5, JETS results in improved SSIM values and reduced aliasing artifacts, when compared to the reconstruction without k_y shifting.

3.4. Analysis of reconstruction parameters

Here we provide a systematic analysis of the proposed JETS reconstruction with LLR regularization applied to the spatial-diffusion dimension, as shown in Fig. 6.

First, we varied the regularization strength λ. We tested values of 0, 0.08, and 0.16. The reconstruction with $\lambda = 0$ in Eq. (7) corresponds to parallel R249.Minor.19 imaging reconstruction without LLR regularization. It is worth noting that the proposed NAViEPI sequence demonstrates high-quality sub-millimeter DW images ($0.5 \times 0.5 \times 2.0$ mm^3 in this example). The DW images can be further improved with the use of LLR regularization, i.e., reduced noise, as seen in the reconstruction with $\lambda = 0.08$. Increasing λ (e.g. 0.16) further reduces noise, but at the cost of increased blurring. Therefore, $\lambda = 0.08$ was selected in this work.

Second, besides the regularization strength, the block size (i.e., the area of 2D patches) also plays a role in denoising. We employed square blocks in

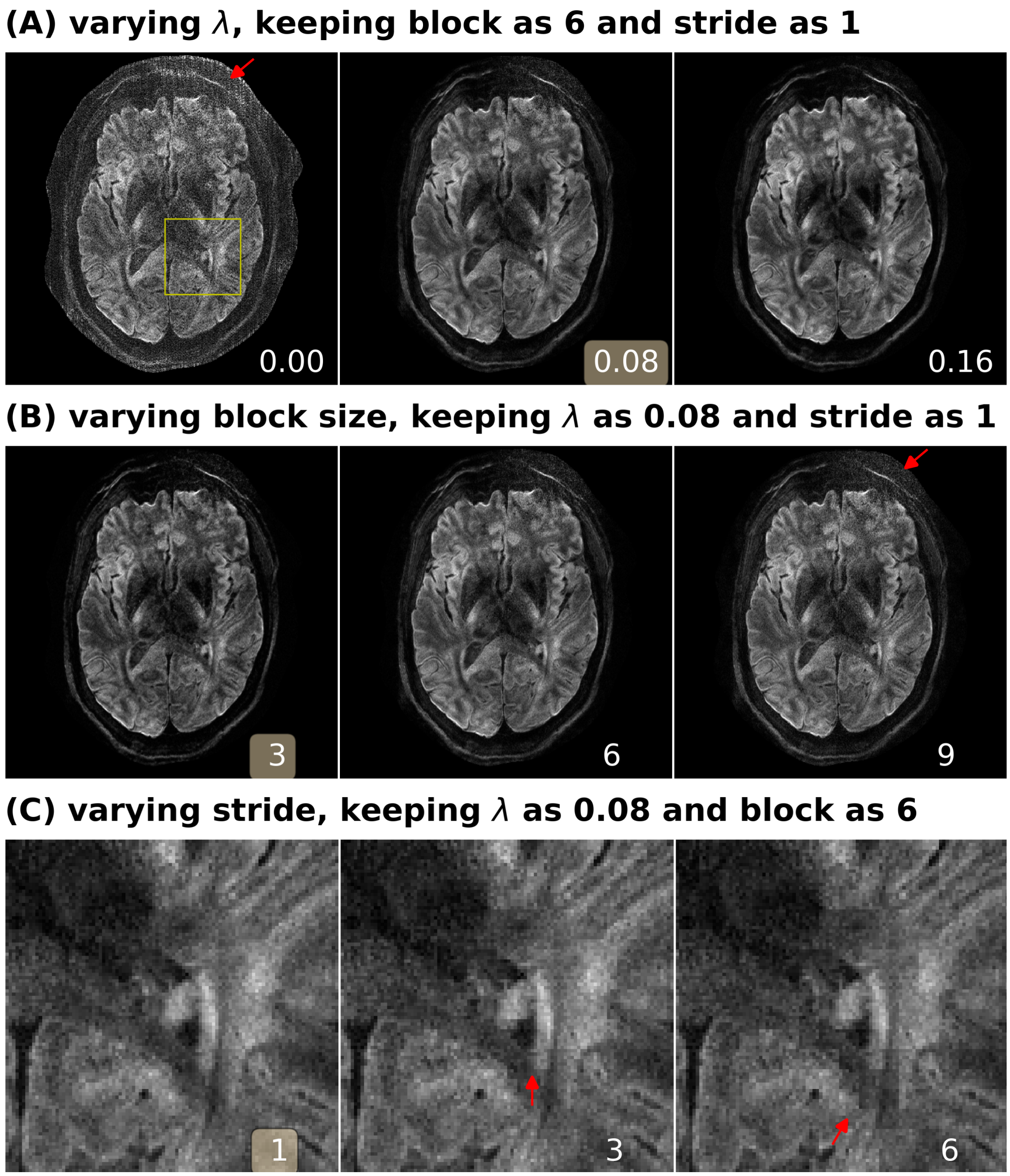

Figure 6: Analysis of reconstruction parameters based on the 3-scan trace acquisition with $0.5 \times 0.5 \times 2.0$ mm^3 (Protocol #3 in Table 1). Displayed are JETS reconstructed single-direction DW images. **(A)** Varying the regularization strength λ from 0 to 0.08 and 0.16. **(B)** Varying the block size from 3 to 6 and 9. **(C)** Varying the stride size from 1 to 3 and 6 (non-overlapping).

this work. Here, the block width of 2 shows the best denoising as compared to 1 and 3, especially in the peripheral brain region. Among the three tested block widths, the block size of 4 (with the block width 2) is the smallest one which is no smaller than the diffusion directions in this 3-scan trace example (1 b_0 plus 3 orthogonal diffusion directions). This observation agrees with the suggestion that the patch size should be no smaller than and close to the diffusion directions (Cordero-Grande et al., 2019).

Third, we varied the stride, i.e., the step from one local patch to the next. The use of overlapping LLR (Fig. 6 (C) left) better suppresses blocky artifacts, compared to the partially overlapping LLR (Fig. 6 (C) middle) and R248.Major.4b the non-overlapping LLR (Fig. 6 (C) right).

3.5. Sampling efficiency of NAViEPI

As shown in Fig. 7, NAViEPI achieves sub-millimeter resolution (voxel size $0.5\times0.5\times2.0\ \text{mm}^3$) with the use of a 5-shot acquisition. When compared to a single-shot acquisition with the same voxel size, the acquisition time of R249.Minor.22 NAViEPI is about two times longer, but the image quality of NAViEPI is remarkably improved.

In the sub-millimeter imaging scenario, the increased base resolution requires longer TE (143 ms) in the single-shot acquisition, which results in significant signal loss due to T_2 relaxation. Therefore, sub-millimeter DWI necessitates multi-shot acquisition, which is subject to shot-to-shot phase variation and long scan time. However, NAViEPI solves both challenges. The 5-shot acquisition reduces TE to 58 ms, and thus retains SNR significantly compared to the single-shot acquisition. Moreover, the JETS reconstruction can help to reduce noise and improve structural visibility.

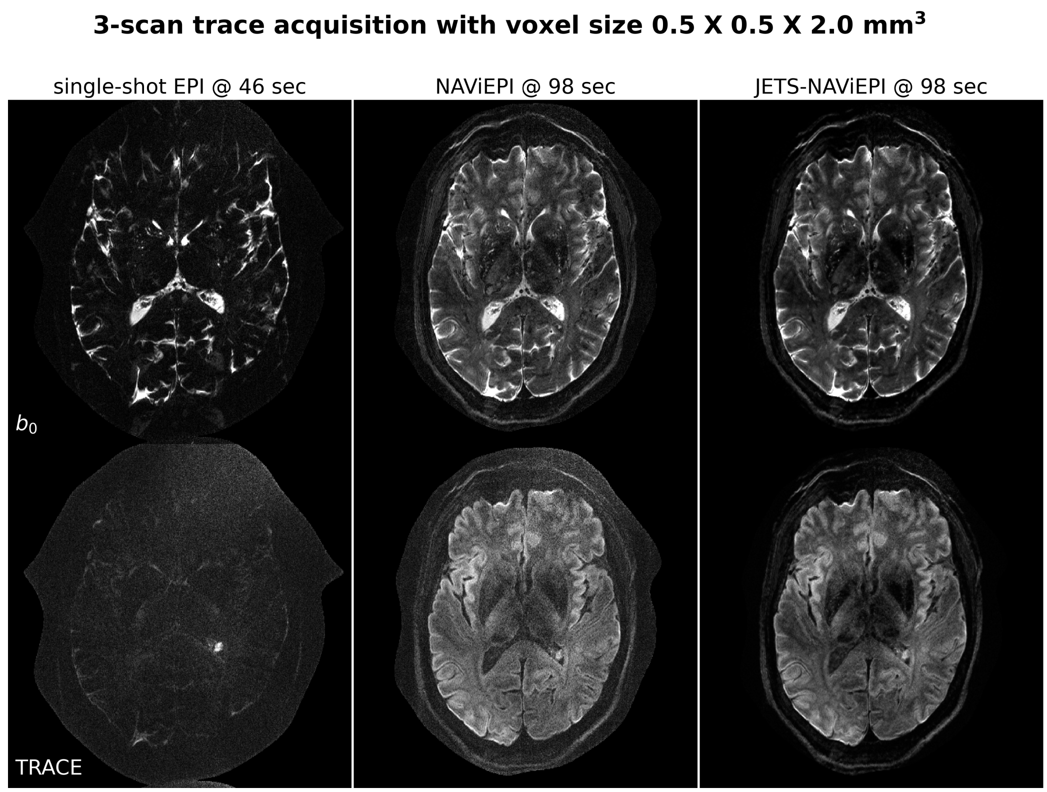

Figure 7: Sampling efficiency of the proposed NAViEPI sequence. 5-shot NAViEPI acquisition with the voxel size $0.5 \times 0.5 \times 2.0$ mm^3 (Protocol #3) was compared with single-shot EPI acquisition (Protocol #4). Both the 1st and the 2nd columns were reconstructed via parallel imaging without LLR regularization, whereas the 3rd column was reconstructed via JETS.

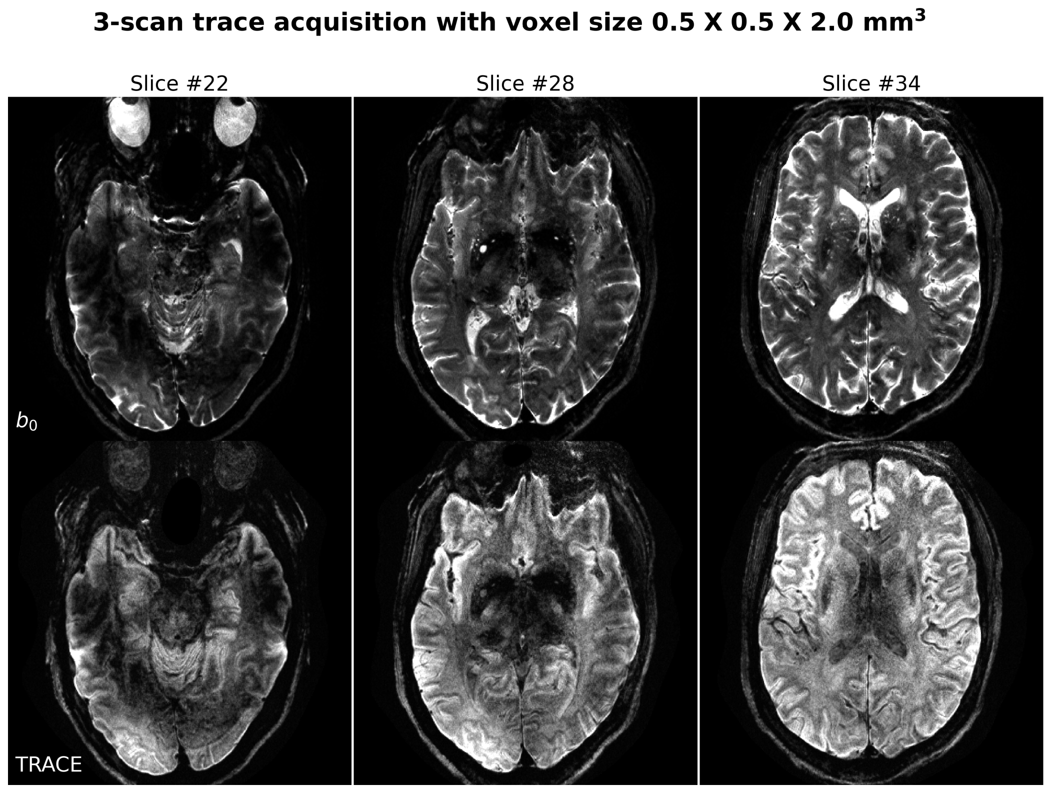

Figure 8: Reconstruction of the 3-scan trace acquisition with the voxel size $0.5 \times 0.5 \times 2.0$ mm^3 (Protocol #3) at different slices.

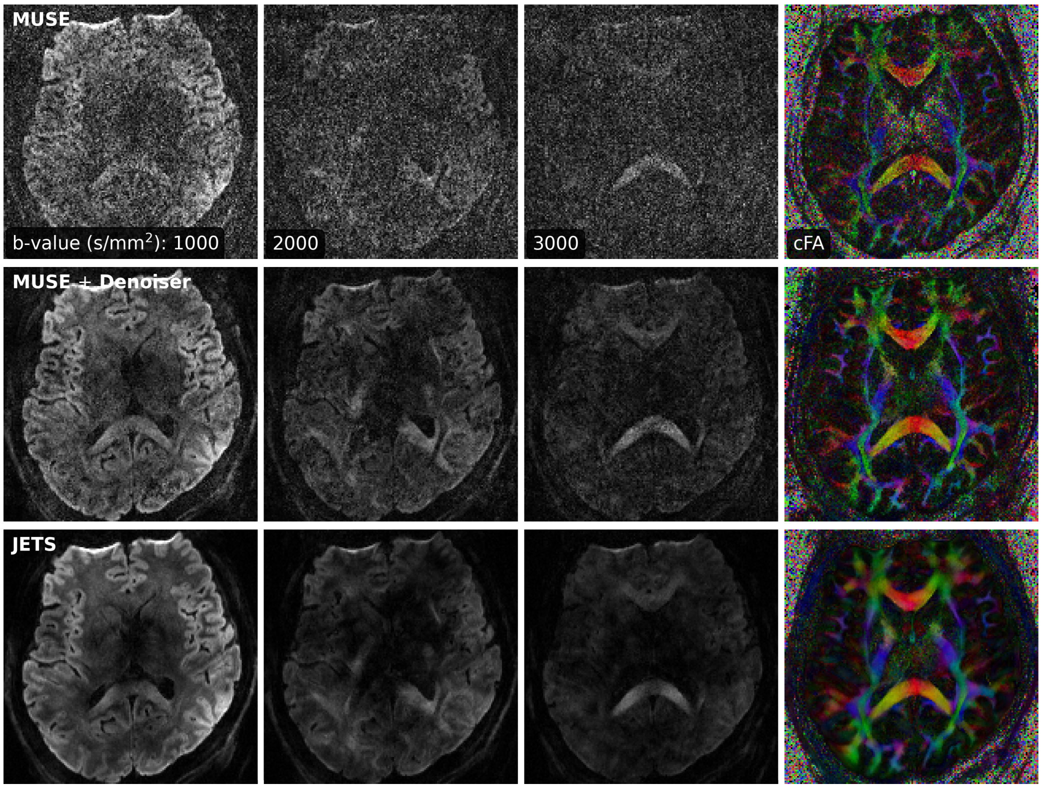

Figure 9: Comparison of three-shell DWIs and cFA maps with data acquired by Protocol #2 in Table 1. Reconstruction methods from top to bottom were MUSE, MUSE with the local-PCA denoiser, and the proposed JETS method.

Fig. 8 shows the JETS reconstructed b_0 and TRACE images in different slice locations. Admittedly, the lower brain region (e.g. slice #22) exhibits inhomogeneous and lower signal intensity than the upper slices. Such inhomogeneity can be alleviated with the use of multi-channel parallel transmission (Katscher et al., 2003; Grissom et al., 2010).

3.6. Diffusion tensor imaging

Protocol #2 in Table 1 yields an acceleration factor of 6×3 per shot, resulting in severe noise amplification in MUSE reconstructed DWIs, as shown in Fig. 9. The local-PCA denoiser substantially removes noise, but the DWI at high b-values still illustrates more noise, compared to the proposed JETS reconstruction.

4. Discussion

This work reports a novel DW-MRI technique, JETS-NAViEPI. NAViEPI (1) achieves the fast and efficient acquisition of both imaging and navigator echoes, (2) enforces consistent effective ESP between the two echoes, and (3) allows for undersampled iEPI as well as a large number of shots. Moreover, compared to the single-shot acquisition, joint k-q-slice reconstruction with k_y-shift encoding on NAViEPI retains SNR and reduces aliasing artifacts in DW images. As a result, JETS-NAViEPI renders high spatiotemporal resolution diffusion MRI protocols in 7 T, e.g., a 3-scan trace acquisition with the voxel size $0.5 \times 0.5 \times 2.0$ mm^3 at 1.5 min. R249.Minor.24

One limitation of JETS-NAViEPI is the long reconstruction time due to the simultaneous reconstruction of all DW images and the use of overlapping locally low-rank regularization. The reconstruction for the Protocol #3 in Table 1 on an A100 GPU takes about 2 min per multi-band slice. To reduce the computation time, coil compression algorithms (Buehrer et al., 2007; Huang et al., 2008) can be employed to reduce the number of coils for image reconstruction. Moreover, one can deploy multi-GPU distributed computing or modern optimization algorithms (e.g. stochastic gradient descent) (Ong et al., 2020) to speed up the reconstruction.

Neither the signal modeling in Eqs. (2) and (4) nor the LLR regularization considers the subject motion. In the presence of motion, the regularized reconstruction can degrade. To overcome this problem, scout-informed motion estimation and reconstruction (Polak et al., 2022) could be integrated into the framework.

Another potential extension of this work is to incorporate distortion correction. The standard distortion correction method is known as TOPUP (Andersson et al., 2003), which acquires two scans with opposing phase-encoding directions to obtain the field inhomogeneity map and then performs conjugate phase reconstruction to correct for distortion. Alternatively, the multi-echo acquisition could be used for the coil sensitivity reference scan, R249.Minor.25 such that both coil sensitivity and B_0 field inhomogeneity maps could be reconstructed from the data.

This work employed a single regularization weight λ to enforce low rankness along the spatial-diffusion direction. However, SNR may be heterogeneous within the FOV. Therefore, one single regularization scalar may be inadequate to cover the whole FOV. Beyond this SVT-based reconstruction, one can seek to use machine learning to learn a q-space prior as the regularizer (Hammernik et al., 2018; Lam et al., 2019; Mani et al., 2021). R249.Minor.26

Although NAViEPI employs navigators for the acquisition of shot-to-shot phase variation, it is worth noting that phase behavior depends on several hard-to-control factors such as pulsatile motion, bulk motion, locations within the brain, and diffusion sensitization strength. Therefore, more comprehensive modeling or post-processing such as image registration can be considered in future work.

This work compared LLR regularized JETS to MUSE post-processed by R248.3b the local PCA denoiser (Cordero-Grande et al., 2019). Technically, the LLR regularization is realized by soft thresholding of the singular values of the spatial-diffusion matrices, whereas the denoiser performs hard thresholding. Both approaches demonstrate effective noise removal. In the scenario of accelerated acquisitions, one can employ both approaches to maximally boost

SNR, i.e., the use of LLR regularization for image reconstruction followed by the denoiser as a post-processing step.

While this work reconstructs all DW images and then performs model fitting, an alternative approach is to directly estimate b_0 and diffusion tensors from measured k-q-space data using model-based reconstruction (Knoll et al., 2015; Dong et al., 2018; Shafieizargar et al., 2023). Compared to DW image reconstruction, model-based reconstruction solves for a fewer number of unknowns, but requires strict diffusion tensor modeling and the use of nonlinear least square solvers.

5. Conclusions

We demonstrated the JETS-NAViEPI technique, which integrates a k_y-shifted encoding interleaved EPI sequence and a joint reconstruction with overlapping locally low-rank regularization for high spatial-angular-temporal resolution DW-MRI at 7 T. This technique allows for high-quality DW image reconstruction with accelerated acquisitions.

Funding

Funding by the German Research Foundation (DFG) is gratefully acknowledged (projects 513220538, 512819079; and project 500888779 of the RU5534 MR biosignatures at UHF). In addition, funding by the National Institutes of Health (NIH), R01 EB024532 and P41 EB017183, is gratefully acknowledged.

Data and code available statement

In the spirit of reproducible and open science, we publish our source code (https://github.com/ZhengguoTan/sigpy) as well as the raw k-space data (https://doi.org/10.5281/zenodo.7548595). We also provide interactive demonstrations of the reconstruction procedure (https://github.com/ZhengguoTan/demo_jets_diffusion_mri_7t). R248.8

Acknowledgments

The authors gratefully acknowledge the scientific support and HPC resources provided by the Erlangen National High Performance Computing Center (NHR@FAU) of Friedrich-Alexander-Universität Erlangen-Nürnberg (FAU) under the NHR project b143dc. NHR funding is provided by federal and Bavarian state authorities. NHR@FAU hardware is partially funded by the German Research Foundation (DFG) – 440719683.

The authors thank Dr. Peter Neher for the discussion on MITK-Diffusion. The authors thank Dr. Berkin Bilgic for making the MUSSELS source code (https://bit.ly/2QgBg9U) publically available, Dr. Erpeng Dai for sharing the JULEP source code (https://github.com/daiep/JULEP) on GitHub, and Dr. Zhiyong Zhang for sharing the SPA-LLR source code (https://github.com/ZZgroupSJTU/PMCmsDTI) on GitHub. The authors also thank Dr. Philipp Ehses for the discussion on twixtools (https://github.com/pehses/twixtools).

References

Andersson, J.L.R., Skare, S., Ashburner, J., 2003. How to correct susceptibility distortions in spin-echo echo-planar images: application to diffusion tensor imaging. NeuroImage 20, 870–888. doi:10.1016/S1053-8119(03)00336-7.

Bammer, R., Keeling, S.L., Augustin, M., Pruessmann, K.P., Wolf, R., Stollberger, R., Hartung, H.P., Fazekas, F., 2001. Improved diffusion-weighted single-shot echo-planar imaging (EPI) in stroke using sensitivity encoding (SENSE). Magn. Reson. Med. 46, 548–554. doi:10.1002/mrm.1226.

Basser, P.J., Mattiello, J., Le Bihan, D., 1994. MR diffusion tensor spectroscopy and imaging. Biophys. J. 66, 259–267. doi:10.1016/S0006-3495(94)80775-1.

Bilgic, B., Chatnuntawech, I., Manhard, M.K., Tian, Q., Liao, C., Iyer, S.S., Cauley, S.F., Huang, S.Y., Polimeni, J.R., Wald, L.L., Setsompop, K., 2019. Highly accelerated multishot echo planar imaging through synergistic machine learning and joint reconstruction. Magn. Reson. Med. 82, 1343–1358. doi:10.1002/mrm.27813.

Block, K.T., Uecker, M., Frahm, J., 2007. Undersampled radial MRI with multiple coils. Iterative image reconstruction using a total variation constraint. Magn. Reson. Med. 57, 1186–1098. doi:10.1002/mrm.21236.

Boyd, S., Parikh, N., Chu, E., Peleato, B., Eckstein, J., 2010. Distributed optimization and statistical learning via the alternating direction method of multipliers. Foundations and Trends in Machine Learning 3, 1–122. doi:10.1561/2200000016.

Breuer, F.A., Blaimer, M., Heidemann, R.M., Mueller, M.F., Griswold, M.A., Jakob, P.M., 2005. Controlled aliasing in parallel imaging results in higher acceleration (CAIPIRINHA) for multi-slice imaging. Magn. Reson. Med. 53, 684–691. doi:10.1002/mrm.20401.

Buehrer, M., Pruessmann, K.P., Boesiger, P., Kozerke, S., 2007. Array compression for MRI with large coil arrays. Magn. Reson. Med 57, 1131–1139. doi:10.1002/mrm.21237.

Butts, K., Riederer, S.J., Ehman, R.L., Thompson, R.M., Jack, C.R., 1993. Interleaved echo planar imaging on a standard MRI system. Magn. Reson. Med. 31, 67–72. doi:10.1002/mrm.1910310111.

Cai, J.F., Candès, E.J., Shen, Z., 2010. A singular value thresholding algorithm for matrix completion. SIAM. J. Optim. 20, 1956–1982. doi:10.1137/080738970.

Chen, N.K., Guidon, A., Chang, H.C., Song, A.W., 2013. A robust multi-shot scan strategy for high-resolution diffusion weighted MRI enabled by multiplexed sensitivity-encoding (MUSE). NeuroImage 72, 41–47. doi:10.1016/j.neuroimage.2013.01.038.

Cordero-Grande, L., Christiaens, D., Hutter, J., Price, A.N., Hajnal, J.V., 2019. Complex diffusion-weighted image estimation via matrix recovery under general noise models. NeuroImage 200, 391–404. doi:10.1016/j.neuroimage.2019.06.039.

Dai, E., Ma, X., Zhang, Z., Yuan, C., Guo, H., 2017. Simultaneous multislice accelerated interleaved EPI DWI using generalized blipped-CAIPI acquisition and 3D K-space reconstruction. Magn. Reson. Med. 77, 1593–1605. doi:10.1002/mrm.26249.

Dai, E., Mani, M., McNab, J.A., 2023. Multi-band multi-shot diffusion MRI reconstruction with joint usage of structured low-rank constraints and explicit phase mapping. Magn. Reson. Med. 89, 95–111. doi:10.1002/mrm.29422.

Dai, E., Zhang, Z., Ma, X., Dong, Z., Li, X., Xiong, Y., Yuan, C., Guo, H., 2018. The effects of navigator distortion and noise level on interleaved EPI DWI reconstruction: a comparison between image- and k-space method. Magn. Reson. Med. 80, 2024–2032. doi:10.1002/mrm.27190.

Dong, Z., Dai, E., Wang, F., Zhang, Z., Ma, X., Yuan, C., Guo, H., 2018. Model-based reconstruction for simultaneous multislice and parallel imaging accelerated multishot diffusion tensor imaging. Med. Phys. 45, 3196–3204. doi:10.1002/mp.12974.

Garyfallidis, E., Brett, M., Amirbekian, B., Rokem, A., van der Walt, S., Descoteaux, M., Nimmo-Smith, I., Contributors, D., 2014. DIPY, a library for the analysis of diffusion MRI data. Front. Neuroinform. 8, 1–17. doi:10.3389/fninf.2014.00008.

Grissom, W.A., Sacolick, L., Vogel, M.W., 2010. Improving high-field MRI using parallel excitation. Imaging Med. 2, 675–693. doi:10.2217/IIM.10.62.

Griswold, M.A., Jakob, P.M., Heidemann, R.M., Nittka, M., Jellus, V., Wang, J., Kiefer, B., Haase, A., 2002. Generalized autocalibrating partially parallel acquisitions (GRAPPA). Magn. Reson. Med. 47, 1202–1210. doi:10.1002/mrm.10171.

Guhaniyogi, S., Chu, M.L., Chang, H.C., Song, A.W., Chen, N.K., 2016. Motion immune diffusion imaging using augmented MUSE for high-resolution multi-shot EPI. Magn. Reson. Med. 75, 639–652. doi:10.1002/mrm.25624.

Hammernik, K., Klatzer, T., Kobler, E., Recht, M.P., Sodickson, D.K., Pock, T., Knoll, F., 2018. Learning a variational network for reconstruction of accelerated MRI data. Magn. Reson. Med. 79, 3055–3071. doi:10.1002/mrm.26977.

Heidemann, R.M., Porter, D.A., Anwander, A., Feiweier, T., Heberlein, K., Knösche, T.R., Turner, R., 2010. Diffusion imaging in humans at 7 T using readout-segmented EPI and GRAPPA. Magn. Reson. Med. 64, 9–14. doi:10.1002/mrm.22480.

Hestenes, M.R., Stiefel, E., 1952. Methods of conjugate gradients for solving linear systems. J. Res. Natl. Bur. Stand. 49, 409–436. doi:10.6028/jres.049.044.

Hu, Y., Wang, X., Tian, Q., Yang, G., Daniel, B., McNab, J., Hargreaves, B., 2020. Multi-shot diffusion-weighted MRI reconstruction with magnitude-based spatial-angular locally low-rank regularization (SPA-LLR). Magn. Reson. Med. 83, 1596–1607. doi:10.1002/mrm.28025.

Huang, F., Vijayakumar, S., Li, Y., Hertel, S., Duensing, G.R., 2008. A software channel compression technique for faster reconstruction with many channels. Magn. Reson. Imaging 26, 133–141. doi:10.1016/j.mri.2007.04.010.

Jeong, H.K., Gore, J.C., Anderson, A.W., 2013. High-resolution human diffusion tensor imaging using 2-D navigated multishot SENSE EPI at 7 T. Magn. Reson. Med. 69, 793–802. doi:10.1002/mrm.24320.

Jones, D.K., 2010. Diffusion MRI: Theory, methods, and applications. Oxford University Press. doi:10.1093/med/9780195369779.001.0001.

Katscher, U., Börnert, P., Leussler, C., van den Brink, J.S., 2003. Transmit SENSE. Magn. Reson. Med. 49, 144–150. doi:10.1002/mrm.10353.

Knoll, F., Raya, J.G., Halloran, R.O., Baete, S., Sigmund, E., Bammer, R., Block, T., Otazo, R., Sodickson, D.K., 2015. A model-based reconstruction for undersampled radial spin-echo DTI with variational penalties on the diffusion tensor. NMR Biomed 28, 353–366. doi:10.1002/nbm.3258.

Lam, F., Li, Y., Peng, X., 2019. Constrained magnetic resonance spectroscopic imaging by learning nonlinear low-dimensional models. IEEE Trans. Med. Imaging 39, 545–555. doi:10.1109/TMI.2019.2930586.

Le Bihan, D., Breton, E., Lallemand, D., Grenier, P., Cabanis, E., Laval-Jeantet, M., 1986. MR imaging of intravoxel incoherent motions: application to diffusion and perfusion in neurologic disorders. Radiology 161, 401–407. doi:10.1148/radiology.161.2.3763909.

Liang, Z.P., 2007. Spatiotemporal imaging with partially separable functions, in: 2007 4th IEEE International Symposium on Biomedical Imaging: From Nano to Macro, pp. 988–991. doi:10.1109/ISBI.2007.357020.

Liu, C., Moseley, M.E., Bammer, R., 2005. Simultaneous phase correction and SENSE reconstruction for navigated multi-shot DWI with non-Cartesian k-space sampling. Magn. Reson. Med. 54, 1412–1422. doi:10.1002/mrm.20706.

Lustig, M., Donoho, D., Pauly, J.M., 2007. Sparse MRI: The application of compressed sensing for rapid MR imaging. Magn. Reson. Med. 58, 1182–1195. doi:10.1002/mrm.21391.

Mani, M., Jacob, M., Kelley, D., Magnotta, V., 2017. Multi-shot sensitivity-encoded diffusion data recovery using structured low-rank matrix completion (MUSSELS). Magn. Reson. Med. 78, 494–507. doi:10.1002/mrm.26382.

Mani, M., Magnotta, V.A., Jacob, M., 2021. qModeL: A plug-and-play model-based reconstruction for highly accelerated multi-shot diffusion MRI using learned priors. Magn. Reson. Med. 86, 835–851. doi:10.1002/mrm.28756.

Mansfield, P., 1977. Multi-planar image formation using NMR spin echoes. J Phys C 10, 55–58. doi:10.1088/0022-3719/10/3/004.

Maudsley, A.A., 1980. Multiple-line-scanning spin density imaging. J. Magn. Reson. 41, 112–126. doi:10.1016/0022-2364(80)90207-3.

Merboldt, K.D., Hanicke, W., Frahm, J., 1985. Self-diffusion NMR imaging using stimulated echoes. J. Magn. Reson. 64, 479–486. doi:10.1016/0022-2364(85)90111-8.

Mori, S., Crain, B.J., Chacko, V.P., Van Zijl, P.C.M., 1999. Three-dimensional tracking of axonal projections in the brain by magnetic resonance imaging. Ann. Neurol. 45, 265–269. doi:10.1002/1531-8249(199902)45:2<265::AID-ANA21>3.0.CO;2-3.

Ong, F., Lustig, M., 2019. SigPy: A Python package for high performance iterative reconstruction, in: Proceedings of the 27th Annual Meeting of ISMRM, Montréal, CAN, p. 4819. doi:10.5281/zenodo.5893788.

Ong, F., Zhu, X., Cheng, J.Y., Johnson, K.M., Larson, P.E.Z., Vasanawala, S.S., Lustig, M., 2020. Extreme MRI: Large-scale volumetric dynamic imaging from continuous non-gated acquisitions. Magn. Reson. Med. 84, 1763–1780. doi:10.1002/mrm.28235.

Pipe, J.G., Farthing, V.G., Forbes, K.P., 2002. Multishot diffusion-weighted FSE using PROPELLER MRI. Magn. Reson. Med. 47, 42–52. doi:10.1002/mrm.10014.

Polak, D., Splitthoff, D.N., Clifford, B., Lo, W.C., Huang, S.Y., Conklin, J., Wald, L.L., Setsompop, K., Cauley, S., 2022. Scout accelerated motion estimation and reduction (SAMER). Magn. Reson. Med. 87, 163–178. doi:10.1002/mrm.28971.

Porter, D.A., Heidemann, R.M., 2009. High resolution diffusion-weighted imaging using readout-segmented echo-planar imaging, parallel imaging and a two-dimensional navigator-based reacquisition. Magn. Reson. Med. 62, 468–475. doi:10.1002/mrm.22024.

Pruessmann, K.P., Weiger, M., Scheidegger, M.B., Boesiger, P., 1999. SENSE: Sensitivity encoding for fast MRI. Magn. Reson. Med. 42, 952–962. doi:10.1002/(SICI)1522-2594(199911)42:5<952::AID-MRM16>3.0.CO;2-S.

Ra, J.B., Rim, C.Y., 1993. Fast imaging using subencoding data sets from multiple detectors. Magn. Reson. Med. 30, 142–145. doi:10.1002/mrm.1910300123.

Roemer, P.B., Edelstein, W.A., Hayes, C.E., Souza, S.P., Mueller, O.M., 1990. The NMR phased array. Magn. Reson. Med. 16, 192–225. doi:10.1002/mrm.1910160203.

Setsompop, K., Fan, Q., Stockmann, J., Bilgic, B., Huang, S., Cauley, S.F., Nummenmaa, A., Wang, F., Rathi, Y., Witzel, T., Wald, L.L., 2018. High-resolution in vivo diffusion imaging of the human brain with generalized slice dithered enhanced resolution: Simultaneous multislice (gSlider-SMS). Magn. Reson. Med. 79, 141–151. doi:10.1002/mrm.26653.

Setsompop, K., Gagoski, B.A., Polimeni, J.R., Witzel, T., Wedeen, V.J., Wald, L.L., 2012. Blipped-controlled aliasing in parallel imaging for simultaneous multislice echo planar imaging with reduced g-factor penalty. Magn. Reson. Med. 67, 1210–1224. doi:10.1002/mrm.23097.

Shafieizargar, B., Jeurissen, B., Poot, D.H.J., Klein, S., Van Audekerke, J., Verhoye, M., den Dekker, A.J., Sijbers, J., 2023. ADEPT: Accurate diffusion echo-planar imaging with multi-contrast shoTs. Magn. Reson. Med. 89, 396–410. doi:10.1002/mrm.29398.

Tournier, J.D., Smith, R., Raffelt, D., Tabbara, R., Dhollander, T., Pietsch, M., Christiaens, D., Jeurissen, B., Yeh, C.H., Connelly, A., 2019. MRtrix3: A fast, flexible and open software framework for medical image processing and visualisation. NeuroImage 202, 116137. doi:https://doi.org/10.1016/j.neuroimage.2019.116137.

Trzasko, J., Manduca, A., 2011. Local versus global low-rank promotion in dynamic MRI series reconstruction, in: Proceedings of the 19th Annual Meeting of ISMRM, Montréal, CAN, p. 4371.

Tuch, D.S., Reese, T.G., Wiegell, M.R., Makris, N., Belliveau, J.W., Wedeen, V.J., 2002. High angular resolution diffusion imaging reveals intravoxel white matter fiber heterogeneity. Magn. Reson. Med. 48, 577–582. doi:10.1002/mrm.10268.

Uecker, M., Lai, P., Murphy, M.J., Virtue, P., Elad, M., Pauly, J.M., Vasanawala, S.S., Lustig, M., 2014. ESPIRiT – an eigenvalue approach to autocalibrating parallel MRI: Where SENSE meets GRAPPA. Magn. Reson. Med. 71, 990–1001. doi:10.1002/mrm.24751.

Wu, W., Koopmans, P.J., Andersson, J.L., Miller, K.L., 2019. Diffusion Acceleration with Gaussian process Estimated Reconstruction (DAGER). Magn. Reson. Med. 82, 107–125. doi:10.1002/mrm.27699.

Wu, W., Miller, K.L., 2017. Image formation in diffusion MRI: A review of recent technical developments. J. Magn. Reson. Imaging 46, 646–662. doi:10.1002/jmri.25664.

Zhang, T., Pauly, J.M., Levesque, I.R., 2015. Accelerated parameter mapping with a locally low rank constraint. Magn. Reson. Med. 73, 655–661. doi:10.1002/mrm.25161.

Supplementary Information

Accelerated Diffusion Weighted Magnetic Resonance Imaging at 7 T: Joint Reconstruction for Shift-Encoded Navigator-based Interleaved Echo Planar Imaging (JETS-NAViEPI)

Zhengguo Tan, Patrick A. Liebig, Robin M. Heidemann, Frederik B. Laun, Florian Knoll

Here we aim to reproduce the results. Another subject was recruited and measured by all protocols listed in Table 1 in the main manuscript.

8th DW image from 4-shot iEPI @ 1 mm ISO

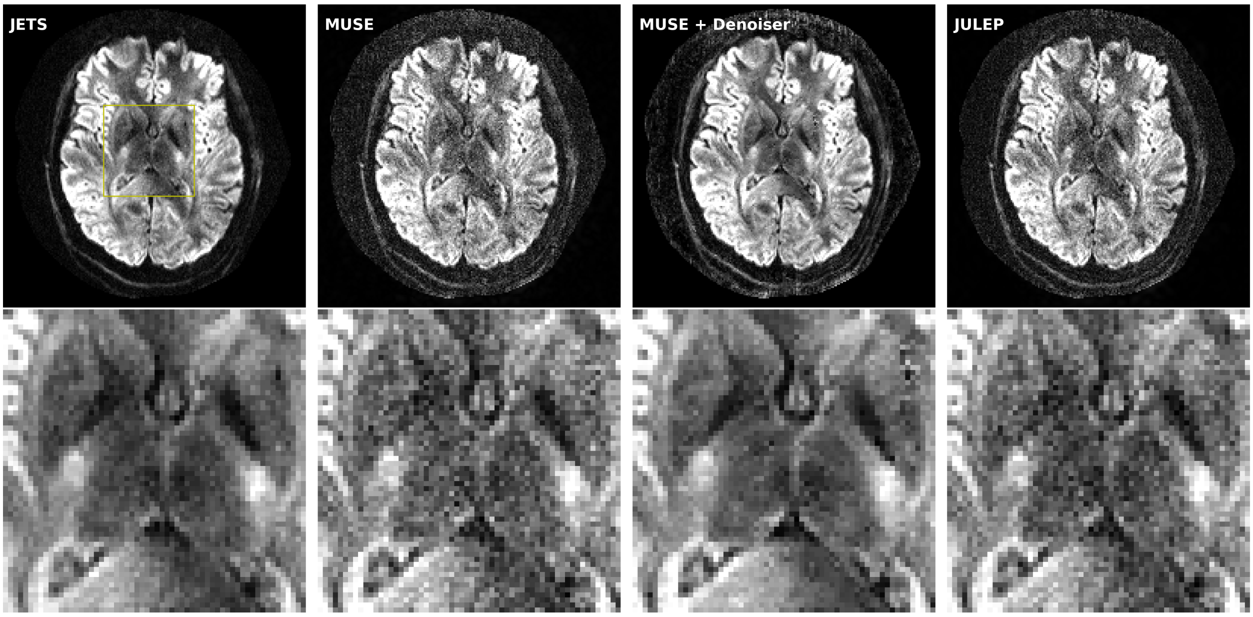

SI Figure S1: Reproducing Protocol #1. Reconstructed DW images (the 8th diffusion encoding) based on 4-shot iEPI acquisition with 1 mm isotropic resolution. Four reconstruction methods are compared (from left to right): JETS, MUSE, MUSE with denoiser, and JULEP. The 2nd row displays the magnified views of the yellow square.

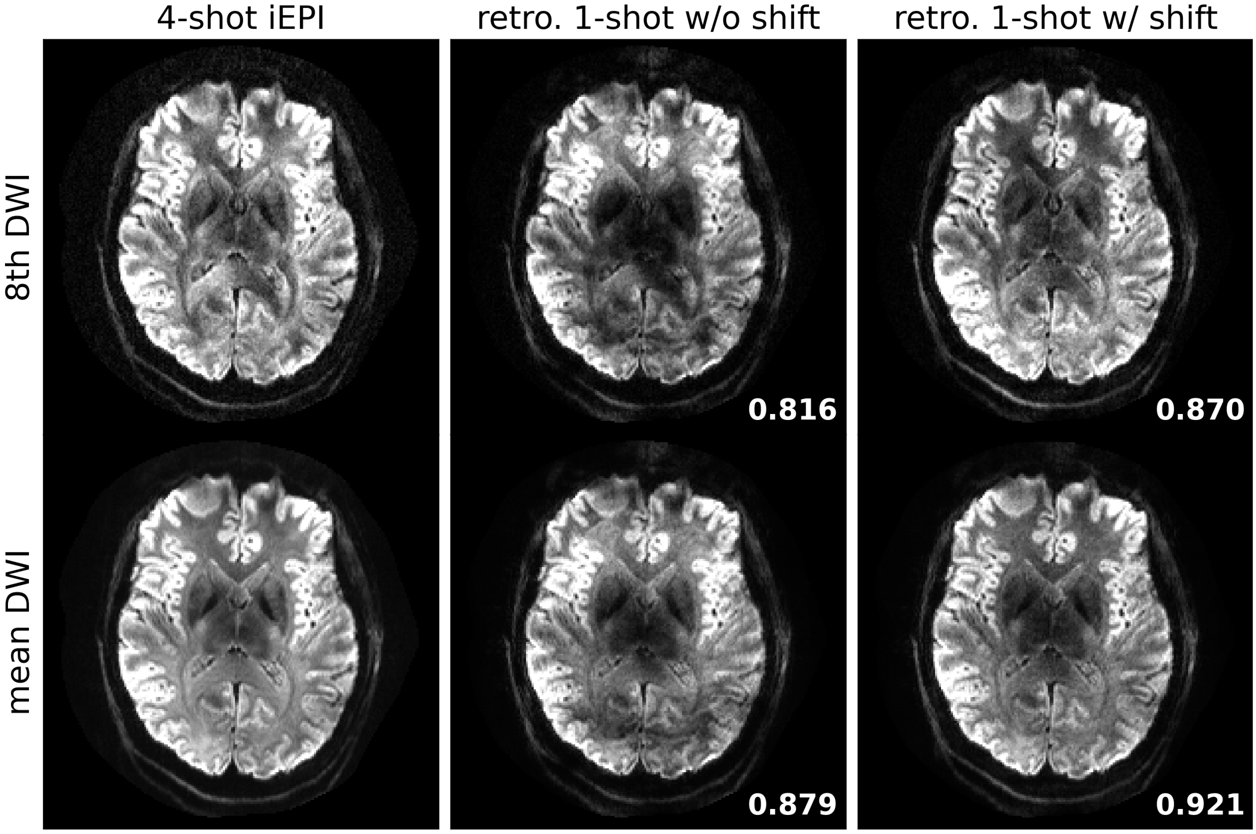

SI Figure S2: Reproducing Protocol #1. Quantitative validation of the proposed k_y-shift enoding sampling pattern based on 4-shot iEPI acquisition with 1 mm isotropic resolution. (Top) the 8th diffusion encoding and (bottom) mean DWI over 20 diffusion encodings. (1st column) JETS reconstruction of 4-shot iEPI acquisition is used as the ground truth. The 2nd and the 3rd column displays JETS reconstruction of retrospectively undersampled 1-shot acquisition without and with k_y shifting, respectively.

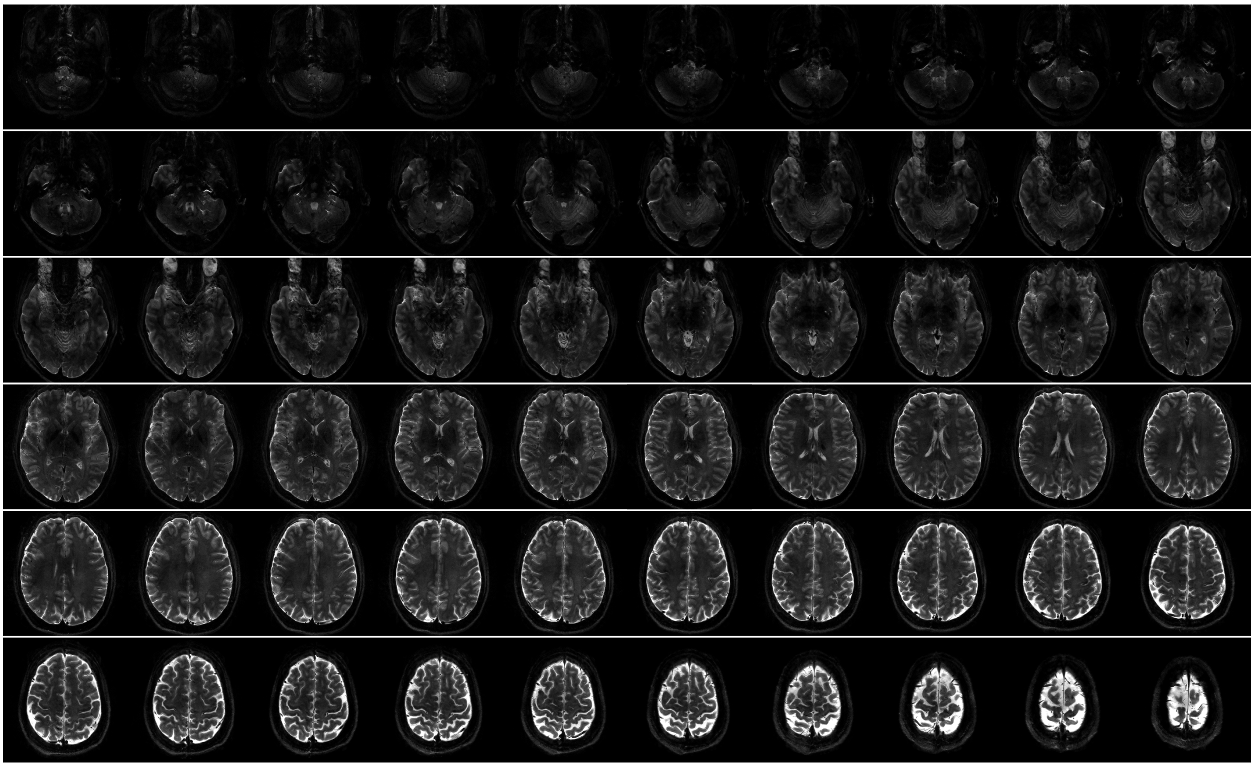

SI Figure S3: Reproducing Protocol #3. Reconstructed b_0 images from the 3-scan trace acquisition with the voxel size $0.5 \times 0.5 \times 2.0$ mm^3.

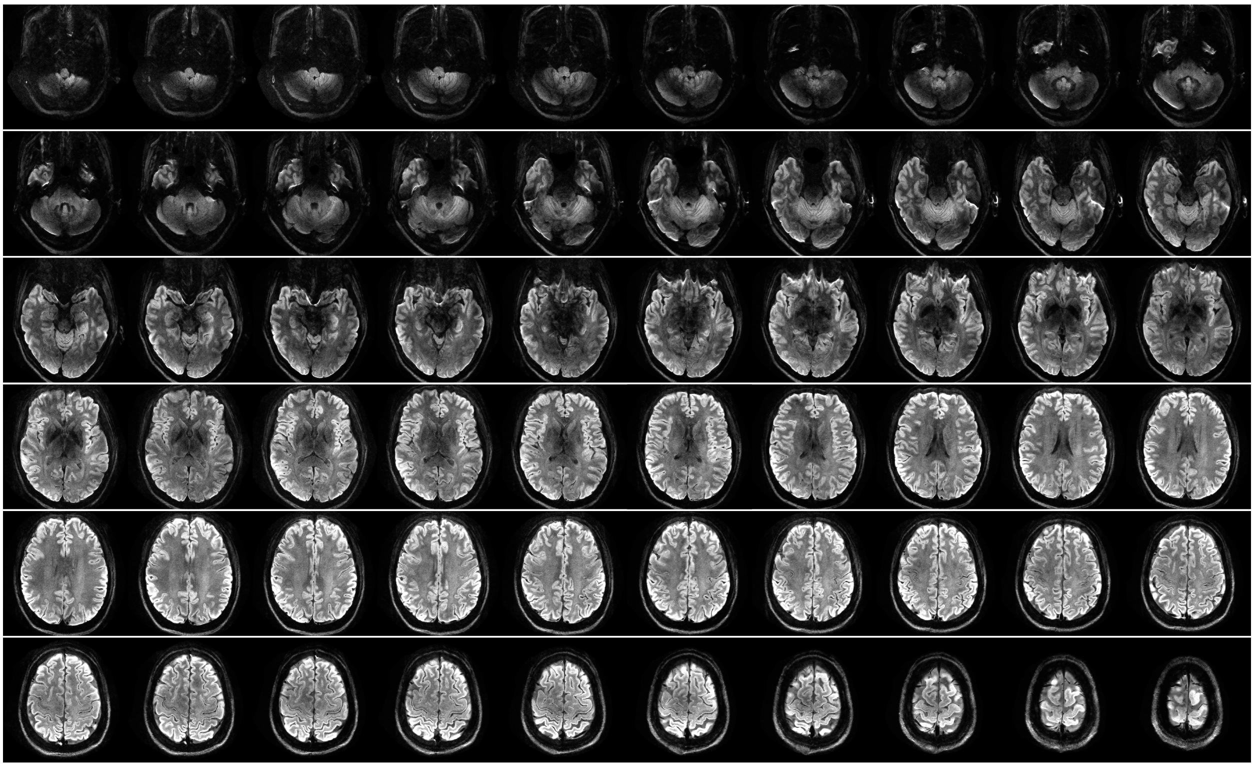

SI Figure S4: Reproducing Protocol #3. Reconstructed TRACE images from the 3-scan trace acquisition with the voxel size $0.5 \times 0.5 \times 2.0$ mm^3.

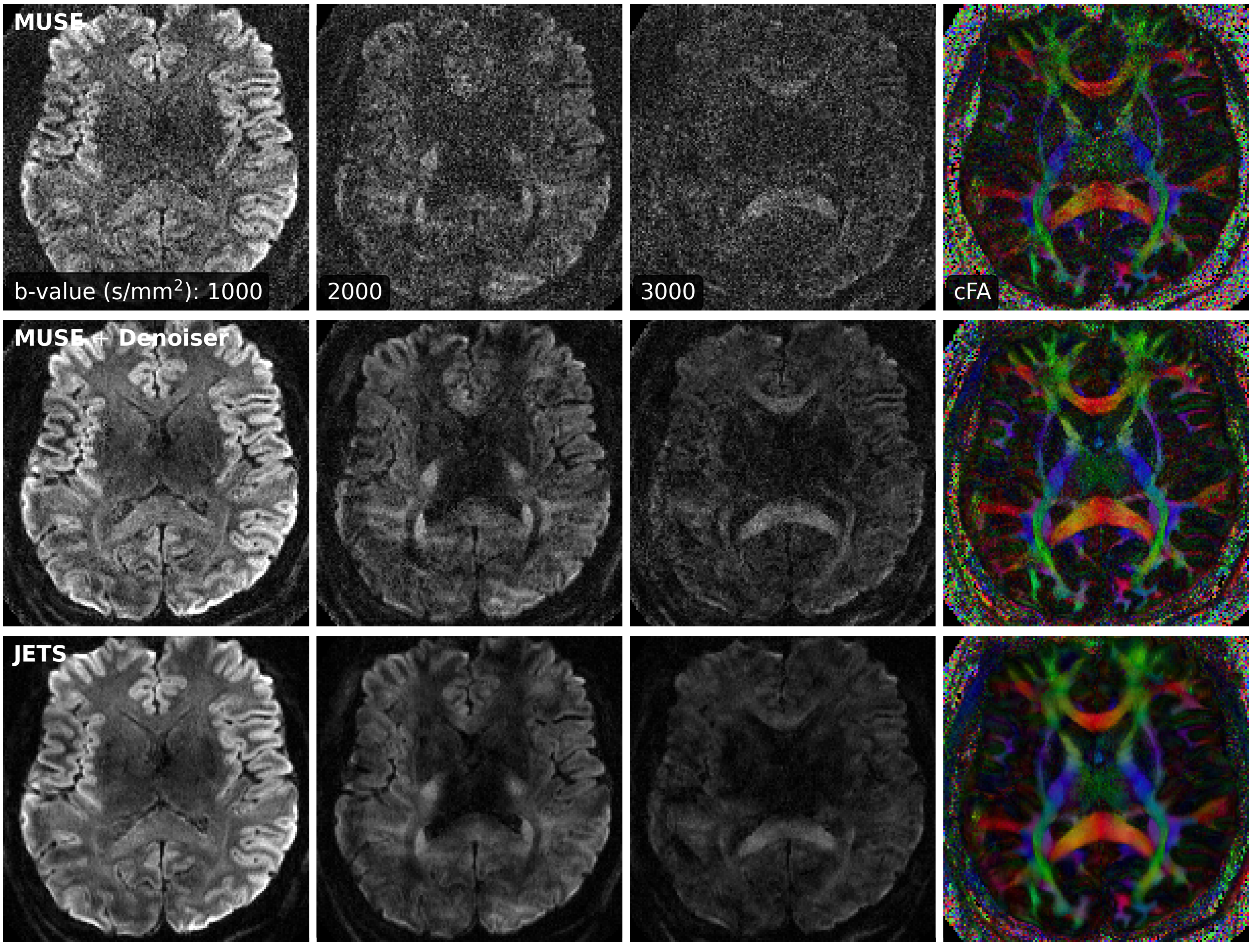

SI Figure S5: Reproducing Protocol #2. The FOV and bandwidth were adapted as $200\,\mathrm{mm}$ and 1086 Hz/pixel, respectively. Comparison of three-shell DWIs and cFA maps reconstructed by (top to bottom) MUSE, MUSE with the local-PCA denoiser, and the proposed JETS method, respectively.

Imaging Neuroscience #203: Responses to Editors and Reviewers

Reviewer #248

Authors have partially addressed my previous comments. A list of pending issues is listed below:

Major:

1) *The experiment is generally satisfactory, but its description is a bit confusing (especially point b) below:*

   a) *L125: "Protocol #1 with six-shot iEPI and without in-plane undersampling was implemented" then (L131) "We then retrospectively reduced the four-shot data to only one shot", guess there is a misprint in L125 which should be four-shot rather than six-shot?*

   b) *L132: "with the proposed k_y shifting to simulate three-fold in-plane undersampling" $\rightarrow$ as there is no in-plane undersampling in Protocol #1 in the baseline data (according to Table 1) this sounds a bit confusing, if 1 out of 4 shots are used this would be four-fold in-plane undersampling, so unclear how you reach three-fold in-plane undersampling? Guess you mean something like "three-fold in-plane interleaving"? A few more details may help here.*

   c) *L133: "JETS reconstruction was performed on all data" $\rightarrow$ "all data" is a bit vague, please reword.*

   a) Sorry about the misprint. We corrected it as four-shot.

   b) Thank you for the question. You are right that "1 out of 4 shots are used", so it is four-fold in-plane undersampling. We corrected this in the manuscript.

   c) Thank you. This sentence has been reworded.

2) *Fine, only a small detail, L61: "acquisition. SPA-LLR" $\rightarrow$ "acquisition and SPA-LLR"*

   Done.

3) *There are some pending issues:*

   a) *Authors could drop a line in text indicating why they use JULEPS rather than MUSSELS.*

   b) *Results of MUSE + Denoiser look stronger than with previous denoiser. Indeed, now they are quite comparable to JETS (bit noisier but also bit sharper). A question is whether complex denoiser is applied before (replacing TV) or after shot-combination of MUSE? May make sense to try both approaches. Also, authors may want to draw a few lines about potential synergies between their LLR and the denoiser.*

   c) *In previous version you also included comparisons for FA and different b-values but these seem missing here. I think that maintaining comparisons at different b-vals could be particularly useful.*

a) Done.

b) The complex denoiser is applied after the shot combination in MUSE. The local-PCA denoiser operates on spatial-diffusion matrices, whereas MUSE reconstructs one DWI at a time. Therefore, the denoiser is only applicable after the reconstruction of all DWIs, and is not possible before the completion of MUSE (e.g. before shot combination). We added "potential synergies between their LLR and the denoiser" into Discussion.

c) We added back the three-shell data.

4) *Description of these experiments is misleading at times:*

   a) *L300: "According to (Cordero-Grande et al., 2019), it is suggested to keep the patch size roughly equal to the diffusion encoding length. In this 3-scan trace acquisition example, the diffusion encoding length is 4 (1 b0 plus 3 orthogonal diffusion directions). Among the tested block sizes, 3 is the closest to 4, and hence renders better denoising"* $\rightarrow$ *but in (Cordero-Grande et al., 2019), patch sizes are automatically estimated (have tried to find suggestion reported without success); whilst patch sizes inducing close to square matrices could be intuitively better for large matrices, that's not so clear for small matrices as here (4 columns); however, even in this case, patch sizes would be width*height, but here they are used interchangeably with widths. All of this needs detailed clarification or another thought.*

   b) *L311: "which is prone to checkerboard artifacts even with the use of random shifting (Saucedo et al., 2017) in each ADMM iteration"* $\rightarrow$ *please review, as message of (Saucedo et al., 2017) seems different: "This result shows the robustness of the LLR-IRPA strategy, which maintains improved computational efficiency compared to CLEAR without introducing block artifacts", i.e., their method shows similar levels of artifacts than overlapped approaches (they even report a reduction in some experiments) / P24(L308): "the increment from one local patch to the next"* $\rightarrow$ *perhaps replace increment by "step" or "distance" for clarity?*

   a) Please refer to your minor comment 9) for responses.

   b) Thank you for the suggestion. We agreed that LLR-IRPA improves the reconstruction for non-overlapping blocks. In our ablation experiments, the use of overlapped LLR better suppresses blocky artifacts. We rewrote this part.

6) *Abstract looks better now, but you may add a one-sentence summary of experimental results. Also, "developed the* k_y*"* $\rightarrow$ *"developed a* k_y*".*

   Thank you. We added the summary of experimental results in Abstract.

7) *Still unclear how do you select the slice / diffusion encoding of snapshots provided in Figs. 4-9. Also, caption of Fig. 5, "retrospecitvely"* $\rightarrow$ *"retrospectively"*

We tried to select representative slices. Figures 4 and 5 show a slice containing the globus pallidus with strong T_2-weighted contrast. Figure 6 selects a slice with a suspicious lesion (the circular bright spot) within the left ventricle. Figure 8 displays three representative slices: (left) the lower brain region which identifies the B_1^+ field inhomogeneity, (middle) the middle brain slice which shows susceptibility artifacts in the frontal region, and (right) the upper brain slice which shows the ventricle.

8) *Understood regarding raw data. However, regarding source code, you say "we publish our source code (https://github.com/ZhengguoTan/sigpy)" but I see no reference to this work in that link. You may clarify by better documenting the repo / providing entry point of specific methods?*

   Thank you for the comment. All our source codes have been pushed here: https://github.com/ZhengguoTan/sigpy. We will document this repo once the manuscript is accepted.

   For an entry point of the proposed methods, please refer to the interactive demo at https://github.com/ZhengguoTan/demo_jets_diffusion_mri_7t. This earned 2nd Place in the MR-Pub Competition organized by the Reproducible Research Study Group in ISMRM 2023.

Minor:

6) *This comment is not satisfactorily addressed:*

   a) *Sentence "firstly slides [...] matrices" (L202) unclear, requested change ("you should reword and explicitly mention what dimensions are concatenated in rows and columns of matrices") not attended.*

   b) *Reasons for not using 3D patches are not convincing. Authors are referring to SMS as reason behind, but this pertains to acquisition whilst patches are defined on image space, so usage of 3D (for instance to exploit redundancies between adjacent slices) could in principle be possible.*

   a) Thank you for the suggestion. We explicitly defined the spatial and diffusion dimension in the manuscript.

   b) SMS acquires spatially separated slices, which means the slices in the joint reconstruction are not spatially continuous. Therefore, 2D patches are used for joint reconstruction. We removed the statement in the manuscript to avoid misunderstanding. But we agreed that after the reconstruction of all slices, 3D-patch-based denoising can be used as a postprocessing step. We put this into Discussion. On the other hand, please refer to the figure in https://github.com/ZhengguoTan/demo_jets_diffusion_mri_7t for the illustration of the construction of the forward model in our proposed reconstruction.

7) *Please, use a symbol rather than "input" (L215) for clarity of this expression.*

   Thank you for the suggestion. We replaced "input".

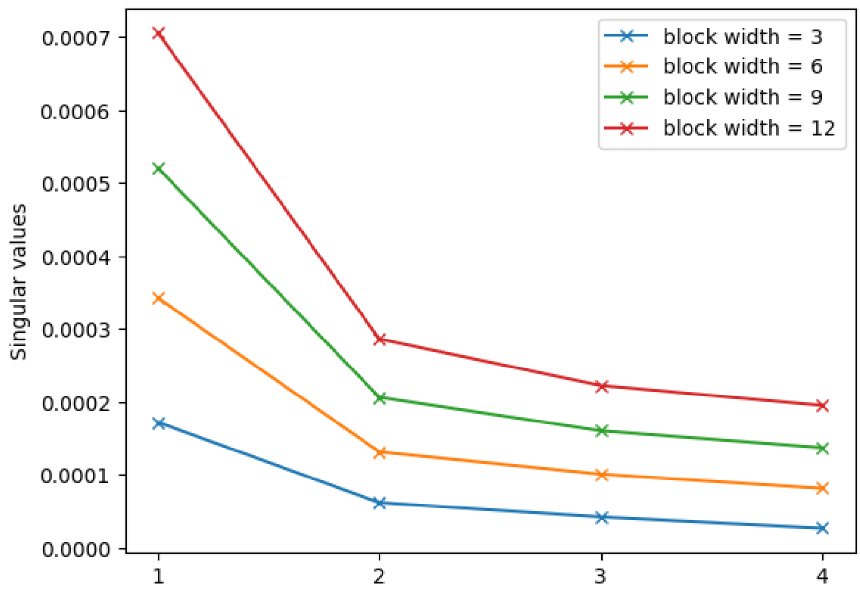

Figure 1: Mean singular values under different block widths. Since square blocks are used here, the block size is equal to the square of the width.

8) *This is only partly attended, when you say "efficient implementation" (L214, L217) → claim on efficiency does not seem supported from description... inverse density weighting is well-known for reconstructing original data levels back when slide-windowing, so this is just the standard method, not something particularly efficient.*

   We removed the "efficiency" statement.

9) *This comment is not satisfactorily addressed. In new Fig. 6b we still see higher noise for larger block sizes, so my previous comment, "may appear counter-intuitive as small block sizes should aid with localization and therefore prevent blurring, at the price of less information for denoising? Can you clarify on reasons / potential hidden factors for this behaviour?" may still be relevant.*

   Very good insight. This is connected to your major comment 4a) and we tried to attend them together.

   Yes, you are right that patch sizes should be width × height. We corrected this in the manuscript.

   The automatic estimation of the block size is described here (`https://mrtrix.readthedocs.io/en/dev/reference/commands/dwidenoise.html`), which suggests selecting "the smallest isotropic patch size that exceeds the number of DW images".

   We provide another notebook for explanations (`https://github.com/ZhengguoTan/demo_jets_diffusion_mri_7t/blob/main/demo_llr.ipynb`). As shown in Figure 1, larger block sizes lead to larger singular values, and thus also result in higher noise when the singular value thresholding value is kept consistent for different block sizes. Therefore, different block sizes require different singular value thresholds.

11) *Sorry, I don't see that this has been attended.*

We added the row "slice thickness" in Table 1.

12) *(New content) Reg. Eq. 6, L. "where the index k denotes the iteration" $\rightarrow$ this iteration was not in previous manuscript, unclear what it refers to.*

It refers to the iteration step of the iterative phase smoothing procedure.

Reviewer #249

I was pleased to see that the Authors have put significant effort into this revision. However some major concerns I had regarding the description of the method and its potential reproducibility still remain.

 # Major

Number of subjects

I am happy that the Authors now state that they measured three subjects in the Methods section, but the presented data still only seem to show a single subject (e.g. in Fig. 9). Perhaps the Authors used a different subject for each separate experiment? Nevertheless, I would really like to see data from more than one subject for each experiment, even if this is put into an Appendix or Supplementary Information. Reproducing results in more than one subject is important to evaluate whether a method gives good results outside of a single (often "best") subject. If the main results do really each rely only on a single subject, I would strongly argue that each result should be reproduced in another subject before publication.

Thank you for your comment. Because of the measurement time constraint, we used a different subject for each separate experiment.

We recruited another subject to reproduce the results. Please refer to Supplementary Information for the results.

Checkerboard artefact suppression (pg. 15)

(1) *I thank the Authors for providing the code that let me understand what the T and T^H operators are doing. However I now think that expressing the operation of T and T^H as matrix multiplication is very misleading. I would urge the Authors to rethink how they express this part. Probably it is e.g. better to write $T(x)$ instead of Tx, unless the authors explicitly define what the multiplication means in this non-standard operation.*

Thank you for looking into the code. We changed to $T(x)$ instead.

(2) *Further, I think T^H needs to be better explained and justified. Where is it used? Are all the blocks reconstructed separately and then recombined for computational efficiency? Or is it just used when calculating the nuclear norm? It seems that T^H is notation from the python package used by the Authors, but I think it is not very useful notation for those unfamiliar with that package. If I followed everything correctly, then what is really needed is an inverse of T (i.e. T^{-1}), but this is non-unique for overlapping blocks (one could have any combination of weights to recombine the overlapping elements as long as they sum to one). The Authors decided to take equal weights for each repeated elements, i.e. to take the mean, and I agree that this is probably the best choice to avoid checkerboard artefacts. However it would be much clearer (at least to me) if the authors expressed this in words, making clear that they take the mean of the overlapping elements, rather than in terms of an operator "T^H" and "multiplication" operations which are not defined by the Authors. The Authors could then*

point explicitly to the scripts they have written for details.

First, the singular value thresholding (nuclear norm regularization) is calculated from the blocks, i.e., $T(x)$. Second, after the thresholding, T^H is used to recombine the blocks to obtain the updated DW images.

(3) *If the operations really do need to be expressed in such detail, then it would perhaps be good to be explicit that the operation to get the "divisor" just gives the element-wise denominator for the mean.*

Thank you for the suggestion. We reworded the description.

(4) *The claim that this way of recombining blocks is efficient is not proven. I would suggest removing this claim.*

OK. We removed this statement.

 # Minor

My minor comments are mainly regarding the wording of some of the new text, which doesn't read as natural English to me. There are also some points which I didn't quite understand which the Authors could consider elaborating on further.

Sincerely thank you for your correction on the language. We have corrected all of them and highlighted the correction in the manuscript. Therefore, no response was provided in the following comments concerning language issues.

(5) *pg. 3: Techniques on the correction of...* $\leftarrow$ *Techniques for the correction of...*

(6) *pg. 11: Different reconstruction methods, i.e., JETS, MUSE, and JULEP were compared.* $\leftarrow$ *Different reconstruction methods, specifically JETS, MUSE, and JULEP, were compared.*

(7) *pg. 12: A possibility is to perform magnitude average...* $\leftarrow$ *One possibility is to perform magnitude averaging...*

(8) *pg. 13: This can be incorporated to our formulation...* $\leftarrow$ *This can be incorporated into our formulation...*

(9) *pg. 14: Please define the nuclear norm in Eq. (7). This would probably also help alleviate some of the problems with the description of the checkerboard artefact suppression mentioned above.*

Thank you. We defined the nuclear norm.

(10) *pg. 15: "This work employed blipped-CAIPI SMS (Setsompop et al., 2012), in which spatially separated slices are simultaneously excited and acquired. Therefore, 2D instead of 3D patches were used to construct the spatial-diffusion matrices." I don't understand how it follows from using multiband that 2D patches are used. Wouldn't this apply to all 2D sequences?*

Thank you for pointing this out. Here we reconstructed multiband slices jointly, but the multiband slices are spatially separated. This prohibits the use of 3D patches for the LLR regularization. We removed this part to avoid this confusion.

(11) *pg. 18: As show in Fig. 3...* $\leftarrow$ *As shown in Fig. 3...*

(12) *pg. 18: ...the ripple-like phase artifact disapper after five iterations.* $\leftarrow$ *...the ripple-like phase artifact disappears after five iterations.*

(13) *Fig. 4: Please define what the arrows represent in the image caption.*

Done.

(14) *pg. 21: retrospecitvely* $\leftarrow$ *retrospectively*

(15) *pg. 21: structural* $\leftarrow$ *Structural*

(16) *Fig. 5: Please define what the arrows represent in the image caption.*

Done.

(17) *pg. 22: as pointed* $\leftarrow$ *as indicated*

(18) *pg. 22: On the contrary* $\leftarrow$ *In contrast*

(19) *pg. 22: First, we varied the regularization strength* λ *from 0, to 0.08, and to 0.16.* $\leftarrow$ *First, we varied the regularization strength* λ*. We tested values of 0, 0.08, and 0.16.*

(20) *pg. 22: "i.e., reduced noise" What does this mean? Perhaps you need to be more explicit?*

Done.

(21) *pg. 24: ...with the use of 5-shot acquisition.* $\leftarrow$ *...with the use of a 5-shot acquisition.*

(22) *pg. 24: When compared to the single-shot acquisition...* $\leftarrow$ *When compared to a single-shot acquisition*

(23) *Fig. 8: The TRACE image at the bottom right seems to show aliasing near the bottom. Do you have an explanation for this?*

This may be caused by B_1 field inhmogeneity from the lower brain region.

(24) *pg. 29: ...MRI protocols in 7 T, e.g., 3-scan trace acquisition...* $\leftarrow$ *...MRI protocols at 7 T, e.g., a 3-scan trace acquisition...*

(25) *pg. 30: "The standard distortion correction method is known as TOPUP (Andersson et al., 2003), which acquires two scans with opposing phase-encoding directions to obtain the field inhomogeneity map and then performs conjugate phase reconstruction to correct for distortion." The B0 map does not need to come from TOPUP. Why not just collect a B0 map from multiecho data and incorporate it into the reconstruction? Often the multiecho data used to create SENSE maps for coil combination is used for this purpose.*

Thank you for the suggestion. We added this into Discussion.

(26) *pg. 30: "Beyond this SVT-based machine-learning reconstruction, one may seek to learn a q-space prior as the regularizer..." I don't understand what this sentence is trying to say. Is it a suggestion that machine learning could be used to learn a q-space prior?*

Yes, it is a suggestion that machine learning could be used to learn a q-space prior.

Reviewer #250

All points of my critique have been addressed adequately.

Thank you for your review.